

Discrete Empirical Interpolation Method for nonlinear softening problems involving damage and plasticity

Steffen Kastian, Jannick Kehls, Tim Brepols and Stefanie Reese

*Institute of Applied Mechanics, RWTH Aachen University,
Mies-van-der-Rohe-Str. 1, 52074 Aachen, Germany*

Abstract. Accurate simulations are essential for engineering applications, and intricate continuum mechanical material models are constructed to achieve this goal. However, the increasing complexity of the material models and geometrical properties lead to a significant increase in computational effort. Model order reduction aims to implement efficient methods for accelerating the simulation process while preserving a high degree of accuracy. Numerous studies have already demonstrated the benefits of this method for linear elastic material modeling. However, in the present work, we investigate a two-surface gradient-extended damage-plasticity model. We conducted complex simulations with this model, demonstrating both damage behavior and softening. The POD-based discrete empirical interpolation method (DEIM) is introduced and implemented. To accomplish simulations with DEIM and softening behaviour, we propose the implementation of a reduced form of the arc-length method. Existing research on calculating models with both damage and softening behavior using the DEIM and arc-length method is limited. To validate the methods, two numerical examples are thoroughly investigated in this study: a plate with a hole and an asymmetrically notched specimen. The results show that the proposed methods can create a reduced order model with high accuracy and a significant speedup of the simulation. For both examples, the analysis is conducted in three steps: first, plasticity without damage is examined, followed by damage without plasticity, and finally, the combination of plasticity and damage is investigated.

Keywords: Computational Mechanics, Model Order Reduction, Hyper-reduction, Proper Orthogonal Decomposition, Discrete Empirical Interpolation Method, Arc-length Method

1 Introduction

In the last few decades, the research field of computational mechanics has been majorly advanced to the point where large-scale simulations are performed throughout all engineering industries. These large-scale simulations deal with a wide variety of phenomena such as dam-

age, thermodynamics, fluids, gasses, electromagnetism, or structural analysis. The possibility to run such resource-intensive simulations became feasible when hardware improved to the point where numerical methods could be employed to solve the aforementioned phenomena. For structural analysis, further hardware improvements were used to calculate bigger and more complex structures with increasingly complex underlying material models. This in turn meant that the simulation time also increased more and more.

To be able to increase the complexity even further, different methods are being taken to reduce the computational effort of the simulations. First of all, high-performance clusters are being used by most of the industry to speed up the simulation times of the huge models that need to be evaluated. Secondly, researchers are trying to increase the processor power of the processing units inside these clusters. Gordon Moore, the namesake of Moore's Law, postulated in the 1960s that the number of transistors per fixed cost, power, and area would double every two years and therefore roughly double the computing power of the processing units every two years. For many decades Moore's law could prove true, but in recent years, processing unit manufacturers struggled more and more to meet the improvement predictions suggested by Moore's law [18]. As a response, researchers are now focusing on new ways to increase processing power. Increasing processing power is of course the most obvious way to reduce the simulation time but there is a third measure being taken which is intensely concerned with reducing the amount of effort to obtain a simulation result.

The topic concerned with reducing the computational complexity of underlying mathematical models is called model order reduction (MOR). Model order reduction is not restricted to structural analysis, but rather a topic in almost all research fields where complex mathematical models are being solved numerically. Model order reduction techniques are therefore often investigated in a wide variety of research fields, but due to the mathematical nature of the different techniques, promising methods are quickly adopted.

Looking at model order reduction in the context of structural problems that are being solved by means of the finite element method (FEM), a problem exists in a high-dimensional space in which it needs to be solved. Through projection based model order reduction techniques, one seeks to reduce the problem from the high-dimensional space to a low-dimensional space, in which the problem can be solved much more quickly. After the solution in the reduced order space has been found, it can be projected back onto the original space. Needless to say that this reduction introduces an approximation error that should be kept as small as possible to maintain the validity of the obtained results.

Model order reduction techniques can be categorized in many ways, but according to Benner et al. [4] the two high-level categories for MOR are, firstly, system-theoretic techniques and, secondly, numerical approaches. The first category is concerned with the derivation of a more compact model with the same geometry but a much smaller number of states, whose response

accurately approximates the response of the full model. Approaches of the second category are not intruding on the underlying theory of the model but are rather concerned with the reduction of the complexity of the numerical methods that are used to solve the problem. Techniques from both categories share the overall objective to reduce the computational complexity of a simulation.

This thesis will focus on the second category of MOR techniques with a specific focus on the snapshot-based proper orthogonal decomposition (POD). In this context, snapshot-based means that to reduce a problem, precomputed solutions of the full problem are used to create the basis matrices that are necessary for the projection from the high-dimensional space to the low-dimensional space and vice versa.

Other than the proper orthogonal decomposition, there are different snapshot-based techniques, which are also well-researched and should not be neglected. Such methods are, for example, the proper generalized decomposition, where Chinesta et al. explore the capabilities of the Proper Generalized Decomposition (PGD) in tackling highly multidimensional models, offering an efficient alternative to traditional mesh-based discretization approaches [8], while Nouy studies different formulations of the PDG and introduces a new one called Minimax PGD [21]. A second class is the reduced basis method which Rozza et al. used for Stokes equations in domains with affine parametric dependence [30] and Fares et al. for the electric field integral equation [13]. Further we would like to mention the load dependent Ritz method. Noor et al. used this approach already 1980 for nonlinear analysis of structures [20]. Additionally it is used for predicting the nonlinear dynamic response [16] and dynamic substructuring [19]. These are just a few model reduction methods among many others. Some methods are used primarily in the field of dynamics, whereas others are mostly used in the field of static problems. Hence, constructing direct comparisons between these methods proves challenging; however, a study comparing the load-dependent Ritz method, modal basis method, and proper orthogonal decomposition for structural quasi-static problems revealed that the proper orthogonal decomposition achieved the highest accuracy while significantly reducing CPU time [24]. This finding contributes to the rationale behind selecting the proper orthogonal decomposition as the fundamental basis for this thesis.

Another significant aspect is that one aim of the thesis is the reduction of highly nonlinear problems where iterative solution schemes have to be used. As a result, the aforementioned methods do not lead to speed-ups of the simulation that are desirable. Why this is the case will be explained in section 3. There are, however, methods to speed up the simulations of nonlinear problems, the so-called hyperreduction techniques [31]. A few promising hyperreduction techniques are based on the POD, such as the gappy POD approach [22, 34], the discrete empirical interpolation method (DEIM) [2, 7, 11], and the empirical cubature [15, 29]. Non-intrusive model order reduction techniques, which do not rely on knowledge of the governing equations, are also well recognized to be present. [9, 12, 32]. Such methods often rely on modern tech-

niques from computer science, namely machine learning, deep learning, and neural networks in general.

The POD technique has gained significant attention and has been widely applied in various fields of engineering and science. It offers an effective approach to reduce the computational complexity of high-dimensional problems while preserving the essential characteristics of the system's behavior. By extracting dominant modes or patterns from a set of precomputed solutions, the POD provides a low-dimensional representation that captures the system's essential dynamics. This reduced-order representation can then be used for efficient simulations, optimization, and uncertainty quantification.

In summary, this work will briefly describe the material model in section 2 and the model order reduction techniques in section 3. Results of the accuracy and efficiency of the method are shown in section 4. Through this research, valuable insights and techniques can be gained to enhance the computational efficiency and accuracy of large-scale simulations in engineering and scientific domains.

1.1 Notational convention

The notational convention used throughout the work follows standard tensor notation. Scalars and scalar-valued functions are denoted by regular italic characters in both upper and lower case, e.g., A or a . Vectors and vector-valued functions are represented by bold italic letters in upper and lower case, e.g., \mathbf{B} or \mathbf{b} . Matrices, tensors of the second order, and tensor-valued functions are written in bold characters of either case, e.g., \mathbf{C} or \mathbf{c} . Greek symbols used to denote second-order tensors are written in bold italic, e.g., $\boldsymbol{\varepsilon}$ or $\boldsymbol{\sigma}$. Fourth-order tensors and tensor-valued functions are represented by italic uppercase calligraphic letters, e.g., \mathcal{D} . The transpose of a vector, matrix, or tensor is displayed with the superscript \top (e.g., \mathbf{B}^\top). The operators Grad and Div describe the gradient and divergence of a scalar, vector, or tensor with respect to Lagrangian coordinates. The abbreviation $\mathbf{C}' := \mathbf{C} - \frac{1}{3}\text{tr}(\mathbf{C})\mathbf{I}$ denotes the deviatoric part of a second-order tensor, where \mathbf{I} is the second-order identity tensor, and $\text{tr}(\mathbf{C})$ represents the trace of \mathbf{C} . The determinant of a tensor \mathbf{C} is denoted as $\det(\mathbf{C})$, and the single contraction of a first-order tensor d with a second-order tensor \mathbf{C} is represented as $\mathbf{C}[d]$.

2 Material Model

In the following section, the constitutive model used to investigate the proposed model order reduction approach will be briefly introduced. The material model was developed by Brepols et al. [6] and serves as the finite strain version of the small strain version of the model [5]. In

principle, the material model is based on the micromorphic approach proposed by Forest [14]. The approach of Forest can be seen as a systematic approach to construct high-level gradient material models of already existing 'local' counterparts. The model introduces an additional nodal degree of freedom for the micromorphic damage. The Helmholtz free energy depends on the difference between the global damage and the local damage which can be strongly coupled by a penalty parameter. This approach is chosen to overcome a general problem of conventional continuum mechanical local damage models, where the softening regime is highly dependent on the mesh discretization in a finite element simulation.

Because the model is implemented with finite deformation kinematics, the reference configuration B_0 at time t_0 and the current configuration B_t at time t of a body are differentiated. For the different configurations, the position of a material point is described by the vectors \mathbf{X} and \mathbf{x} , respectively. The current position of a material point can be obtained by adding a displacement vector \mathbf{u} to the position of the material point in reference configuration such that $\mathbf{x} = \mathbf{X} + \mathbf{u}$. Assuming there exists a mapping $\mathbf{x} = \mathcal{X}(\mathbf{X}, t)$, the deformation gradient can be introduced as $\mathbf{F} := \partial\mathcal{X}(\mathbf{X}, t)/\partial\mathbf{X}$. To model elastoplastic material behavior, the deformation gradient is multiplicatively decomposed into the elastic part \mathbf{F}_e and the plastic part \mathbf{F}_p . Because the model includes Armstrong-Frederick type non-linear kinematic hardening, the plastic part of the deformation gradient is further decomposed into the recoverable part \mathbf{F}_{p_e} and the irrecoverable part \mathbf{F}_{p_i} . After these splits, the deformation gradient reads

$$\mathbf{F} = \mathbf{F}_e \mathbf{F}_p \quad \text{with} \quad \mathbf{F}_p = \mathbf{F}_{p_e} \mathbf{F}_{p_i} \quad (1)$$

and from this, the elastic Cauchy-Green deformation tensors are derived as

$$\mathbf{C}_e = \mathbf{F}_e^\top \mathbf{F}_e, \quad \mathbf{C}_{p_e} = \mathbf{F}_{p_e}^\top \mathbf{F}_{p_e}. \quad (2)$$

Having defined these tensors, the Helmholtz free energy is assumed to be

$$\psi = f_{\text{dam}}(D)(\psi_e(\mathbf{C}_e) + \psi_p(\mathbf{C}_{p_e}, \xi_p)) + \psi_d(\xi_d) + \psi_{\bar{d}}(D - \bar{D}, \text{Grad}(\bar{D})) \quad (3)$$

where ψ_e and ψ_p denote the elastic and plastic part of the free energy, respectively. In addition to the recoverable plastic part of the Cauchy-Green deformation tensor, the plastic part of the free energy also depends on the accumulated plastic strain ξ_p . The energy related to damage hardening is stored in ψ_d and the energy related to the micromorphic extension is stored in $\psi_{\bar{d}}$. Furthermore, the damage hardening energy is dependent on the accumulated damage ξ_d and the energy related to the micromorphic extension is dependent on the micromorphic damage variable \bar{D} . Lastly, the scalar-valued weakening function $f_{\text{dam}}(D)$ is introduced. The elastic

energy is chosen as a compressible Neo-Hookean type and reads

$$\psi_e = \frac{\mu}{2} \left(\text{tr } \mathbf{C}_e - 3 - 2 \ln \left(\sqrt{\det \mathbf{C}_e} \right) \right) + \frac{\lambda}{4} \left(\det \mathbf{C}_e - 1 - 2 \ln \left(\sqrt{\det \mathbf{C}_e} \right) \right) \quad (4)$$

with the two Lamé constants μ and λ . The plastic energy is defined as

$$\psi_p = \frac{a}{2} \left(\text{tr } \mathbf{C}_{p_e} - 3 - 2 \ln \left(\sqrt{\det \mathbf{C}_{p_e}} \right) \right) + e \left(\xi_p + \frac{\exp(-f\xi_p) - 1}{f} \right). \quad (5)$$

The material parameters a , e and f are related to kinematic and non-linear Voce isotropic hardening, with another parameter b showing up in the evolution equation of $\dot{\mathbf{C}}_{p_i}$. The energy related to Voce damage hardening is defined as

$$\psi_d = r \left(\xi_d + \frac{\exp(-s\xi_d) - 1}{s} \right) \quad (6)$$

where r and s are the two damage hardening material parameters. The energy of the micromorphic extension reads

$$\psi_{\bar{d}} = \frac{H}{2} (D - \bar{D})^2 + \frac{A}{2} \text{Grad}(\bar{D}) \cdot \text{Grad}(\bar{D}) \quad (7)$$

with the aforementioned penalty parameter H and the parameter A . An internal length scale is introduced into the material as $L := \sqrt{A/H}$ which can be understood as a localization limiter, preventing the aforementioned localization of damage into a zone of vanishing volume. Choosing the penalty parameter to be a very high number allows for a strong coupling between the micromorphic and the local damage variable. The constitutive equations with respect to the reference configuration are based on the Clausius-Duhem inequality in order to fulfill the second law of thermodynamics. The derivation of the constitutive equations is carefully described by Brepols et al. [6] and because it is not the main topic of this thesis, only the resulting equations are given below:

- State laws:

$$\begin{aligned} \mathbf{S} &= f_{\text{dam}}(D) 2 \mathbf{F}_p^{-1} \frac{\partial \psi_e}{\partial \mathbf{C}_e} \mathbf{F}_p^{-\top} \\ &= f_{\text{dam}}(D) \left(\mu (\mathbf{C}_p^{-1} - \mathbf{C}^{-1}) + \frac{\lambda}{2} \left(\frac{\det \mathbf{C}}{\det \mathbf{C}_p} - 1 \right) \mathbf{C}^{-1} \right) \end{aligned} \quad (8)$$

$$a_{0_i} = \frac{\partial \psi_{\bar{d}}}{\partial \bar{D}} = -H(D - \bar{D}) \quad (9)$$

$$\mathbf{b}_{0_i} = \frac{\partial \psi_{\bar{d}}}{\partial \text{Grad}(\bar{D})} = A \text{Grad}(\bar{D}) \quad (10)$$

- Thermodynamic conjugate forces - plasticity:

$$\mathbf{X} = f_{\text{dam}}(D) 2 \mathbf{F}_{p_i}^{-1} \frac{\partial \psi_e}{\partial \mathbf{C}_{p_e}} \mathbf{F}_{p_i}^{-\top} = f_{\text{dam}}(D) a (\mathbf{C}_{p_i}^{-1} - \mathbf{C}^{-1}) \quad (11)$$

$$q_p = f_{\text{dam}}(D) \frac{\partial \psi_p}{\partial \xi_p} = f_{\text{dam}}(D) e (1 - \exp(-f \xi_p)) \quad (12)$$

- Thermodynamic conjugate forces - damage:

$$Y = -\frac{df_{\text{dam}}(D)}{dD} (\psi_e + \psi_p) - \frac{\partial \psi_{\bar{d}}}{\partial D} = -\frac{df_{\text{dam}}(D)}{dD} (\psi_e + \psi_p) - H(D - \bar{D}) \quad (13)$$

$$q_d = \frac{\partial \psi_d}{\partial \xi_d} = r (1 - \exp(-s \xi_d)) \quad (14)$$

- Auxillary stress tensors:

$$\mathbf{Y} = \mathbf{C}\mathbf{S} - \mathbf{C}_p\mathbf{X}, \quad \mathbf{Y}_{\text{kin}} = \mathbf{C}_p\mathbf{X} \quad (15)$$

- Evolution equations are expressed in terms of effective (i.e., 'undamaged') quantities:

$$(\tilde{\bullet}) := \frac{(\bullet)}{f_{\text{dam}}(D)} \quad (16)$$

$$\dot{\mathbf{C}}_p = 2 \dot{\lambda}_p \frac{\sqrt{3/2}}{f_{\text{dam}}(D)} \frac{\tilde{\mathbf{Y}}' \mathbf{C}_p}{\sqrt{\tilde{\mathbf{Y}}' \cdot (\tilde{\mathbf{Y}}')^\top}}, \quad \dot{\mathbf{C}}_{p_i} = 2 \dot{\lambda}_p \frac{b/a}{f_{\text{dam}}(D)} \mathbf{Y}'_{\text{kin}} \mathbf{C}_{p_i} \quad (17)$$

$$\dot{\xi}_p = \frac{\dot{\lambda}_p}{f_{\text{dam}}(D)}, \quad \dot{D} = \dot{\lambda}_d, \quad \dot{\xi}_d = \dot{\lambda}_d \quad (18)$$

- Yield and damage loading function:

$$\Phi_p = \sqrt{3/2} \sqrt{\tilde{\mathbf{Y}}' \cdot (\tilde{\mathbf{Y}}')^\top} - (\sigma_0 + \tilde{q}_p), \quad \Phi_d = Y - (Y_0 + q_d) \quad (19)$$

- Loading / unloading conditions

$$\begin{aligned} \dot{\lambda}_p &\geq 0, & \Phi_p &\leq 0, & \dot{\lambda}_p \Phi_p &= 0 \\ \dot{\lambda}_d &\geq 0, & \Phi_d &\leq 0, & \dot{\lambda}_d \Phi_d &= 0 \end{aligned} \quad (20)$$

Adding the initial yield stress σ_0 and damage threshold Y_0 in equation 19, the material model has twelve material parameters in total ($\lambda, \mu, \sigma_0, a, b, e, f, Y_0, r, s, A, H$) which should be optimally determined from experimental data. Finally, the micromorphic balance equation can be written as

$$\begin{aligned} H(D - \bar{D}) + A \text{Div}(\text{Grad}(\bar{D})) &= 0 \quad \text{in } B_0 \\ \text{Grad}(\bar{D}) \cdot \mathbf{n}_0 &= 0 \quad \text{on } \partial B_0 \end{aligned} \quad (21)$$

Having the micromorphic balance equation at hand as well as the balance of linear momentum

$$\begin{aligned} \text{Div}(\mathbf{FS}) + \mathbf{f}_0 &= 0 & \text{in } B_0 \\ \mathbf{FS}[\mathbf{n}_0] &= \mathbf{t}_0 & \text{on } \partial B_0 \\ \mathbf{u} &= \hat{\mathbf{u}} & \text{on } \partial B_0 \end{aligned} \quad (22)$$

the weak form of the problem can be constructed. This is done via the usual procedure: First, the balance equations are multiplied by the appropriate test functions $\delta \mathbf{u}$ in case of the linear momentum and $\delta \bar{D}$ in case of the micromorphic balance and then integrated over the reference domain B_0 . After that partial integration and the divergence theorem are applied such that the weak form reads:

$$g(\mathbf{u}, \bar{D}, \delta \mathbf{u}) := \int_{B_0} \mathbf{S} \cdot \delta \mathbf{E} \, dV - \int_{B_0} \mathbf{f}_0 \cdot \delta \mathbf{u} \, dV - \int_{\partial B_{0t}} \mathbf{t}_0 \cdot \delta \mathbf{u} \, dA = 0 \quad \forall \delta \mathbf{u} \quad (23)$$

$$h(\mathbf{u}, \bar{D}, \delta \bar{D}) := \int_{B_0} (H(D - \bar{D})\delta \bar{D} - A \text{Grad}(\bar{D}) \cdot \text{Grad}(\delta \bar{D})) \, dV = 0 \quad \forall \delta \bar{D} \quad (24)$$

The weak form is generally nonlinear and must be linearized with respect to the unknowns and solved iteratively. Details about the linearization and subsequent finite element discretization can be found in [6].

Finally, one ends up with a global system of finite element equations which reads

$$\underbrace{\begin{bmatrix} \mathbf{K}_{uu} & \mathbf{K}_{u\bar{D}} \\ \mathbf{K}_{\bar{D}u} & \mathbf{K}_{\bar{D}\bar{D}} \end{bmatrix}}_{\mathbf{K}_T} \underbrace{\begin{Bmatrix} \Delta \mathbf{u} \\ \Delta \bar{D} \end{Bmatrix}}_{\Delta \mathbf{U}} = - \underbrace{\begin{Bmatrix} \mathbf{R}_u + \mathbf{P}_u \\ \mathbf{R}_{\bar{D}} \end{Bmatrix}}_{\mathbf{G}} \quad (25)$$

The abbreviations \mathbf{K}_T for the tangential stiffness matrix, $\Delta \mathbf{U}$ for the incremental unknowns vector, and \mathbf{G} for the residual vector are introduced for later purposes. To get a solution to the problem at hand, the equation system 25 is solved iteratively until convergence is achieved. For further details regarding the individual components of the tangential stiffness matrix \mathbf{K}_{uu} , $\mathbf{K}_{u\bar{D}}$, $\mathbf{K}_{\bar{D}u}$, $\mathbf{K}_{\bar{D}\bar{D}}$ and the residual vector \mathbf{R}_u , \mathbf{P}_u , $\mathbf{R}_{\bar{D}}$ as well as the algorithmic implementation at the Gauss point level, the reader is again kindly referred to the work of Brepols et al. [6]. Because of the complexity of the material model, the computation of the stiffness matrix is fairly expensive. It should be noted at this point that in the present work, solely linear interpolation functions with 8 integration points per element are used. For completeness, the work of Barfusz et al. [3] should be highlighted, in which a single Gauss point formulation was implemented for the material model at hand and it was validated that the reduced integration approach still yields accurate results and can be used to increase the efficiency.

3 Methods

In this chapter we delve into the various methods used to tackle the challenges of the proposed examples. Those methods include Proper Orthogonal Decomposition, Discrete Empirical Interpolation Method (DEIM) and the arc-length method.

The POD is a mathematical technique used to extract a reduced-order representation of a high-dimensional system. This method has found widespread use in mechanics. Although the primary objective is to decrease the time required for solving the system of equations, it is still necessary to establish the complete system.

The Discrete Empirical Interpolation Method (DEIM) is another numerical method that has gained popularity in mechanics. It is a technique used to reduce the computational complexity of large-scale nonlinear systems. The DEIM only requires the calculation of a few key elements, as opposed to the entire system. Its combination with the POD technique makes it a time-efficient approach.

The arc-length method is a numerical technique used to solve nonlinear equations in mechanics. It is used to trace the response of a structure or system as it undergoes nonlinear deformation, particularly in relation to softening and snapback behavior. This method has found wide application in structural engineering, where it is used to analyze the stability of structures under different loads.

3.1 Proper Orthogonal Decomposition

The proper orthogonal decomposition involves the decomposition of a data matrix, D , into its dominant modes or principal components using singular value decomposition (SVD). In our case, we first solve the full system to obtain the different solution vectors $U_i (i = 1, \dots, l)$, which are then used to construct the snapshot matrix, $D = [U_1, U_2, \dots, U_l] \in \mathbb{R}^{n \times l}$. This snapshot matrix is a time series of the state of the system at discrete time intervals with the solution U_i . We then apply SVD to the snapshot matrix $D = \Phi \Sigma V$, where $\Phi = [\Phi_1, \Phi_2, \dots, \Phi_n] \in \mathbb{R}^{n \times n}$ and $V = [v_1, v_2, \dots, v_l] \in \mathbb{R}^{l \times l}$ are orthonormal matrices, and $\Sigma \in \mathbb{R}^{n \times l}$ is a diagonal matrix containing the singular values. The dominant modes or principal components of the system are then truncated from the left singular vectors of the matrix $\Phi_m = [\Phi_1, \Phi_2, \dots, \Phi_m]$. The matrix Φ_m is the so called projection matrix which contains the main characteristics of the system. The galerkin projection projects U_{red} to the approximated full solution \bar{U}

$$U \approx \bar{U} = \Phi_m U_{red} \quad (26)$$

and the stiffness matrix

$$\mathbf{K}_{T\text{red}}(\bar{\mathbf{U}}) = \Phi_m^\top \mathbf{K}_T(\bar{\mathbf{U}}) \Phi_m \quad (27)$$

into a smaller subspace. The reduced solution scheme for each newton iteration i reads

$$\begin{aligned} \mathbf{K}_{T\text{red}}(\bar{\mathbf{U}}^{(i)}) \Delta \mathbf{U}_{\text{red}}^{(i)} &= -\mathbf{G}_{\text{red}}(\bar{\mathbf{U}}^{(i)}) \\ \bar{\mathbf{U}}^{(i+1)} &= \bar{\mathbf{U}}^{(i)} + \Phi_m \Delta \mathbf{U}_{\text{red}}^{(i)} \\ \mathbf{G}_{\text{red}}^\top(\bar{\mathbf{U}}^{(i)}) \Delta \mathbf{U}_{\text{red}}^{(i)} &\leq \textit{tolerance} \\ i &= i + 1. \end{aligned} \quad (28)$$

Overall, the POD method provides a powerful tool for reducing the computational cost of solving high-dimensional systems, allowing researchers to gain insights into the most critical features of the data while reducing the computational complexity.

3.2 Discrete Empirical Interpolation Method

In this chapter, we explore the Discrete Empirical Interpolation Method (DEIM) and its application in the context of computational mechanics.

The DEIM is a numerical technique that has gained significant attention in recent years due to its ability to reduce the computational complexity of large-scale nonlinear systems. It is particularly useful in the context of computational mechanics, where the behavior of materials is often modeled using partial differential equations (PDEs) and solved numerically. It starts by constructing a set of interpolation points that capture the relevant behavior of the system. These points are typically chosen based on the system's response or other relevant criteria. The system's state variables or parameters are then projected onto these interpolation points, resulting in a reduced-dimensional system. One of the key advantages of DEIM is its ability to accurately approximate the system's response using only a small number of interpolation points. This allows for significant reduction in computational costs, making it well-suited for large-scale problems commonly encountered in computational mechanics.

3.2.1 Mathematical formulation

Similar to the previous chapter on POD, preliminary simulations are necessary in this context as well. Given the proficiency of POD in handling linear simulations and the complementary nature of DEIM in addressing nonlinear behavior, we partition the internal force vector $\mathbf{R}(\mathbf{U})$ into distinct linear $\mathbf{R}_{lin}(\mathbf{U})$ and nonlinear $\mathbf{R}_{nl}(\mathbf{U})$ components. This was already proposed by Radermacher and Reese [25] to avoid singular matrices. The linear part is defined as $\mathbf{R}_{lin}(\mathbf{U}) =$

$\mathbf{K}_{lin}\mathbf{U}$ and therefore the nonlinear part results in

$$\mathbf{R}_{nl}(\mathbf{U}) = \mathbf{R}(\mathbf{U}) - \mathbf{K}_{lin}\mathbf{U} \quad (29)$$

where \mathbf{K}_{lin} is the constant stiffness matrix obtained in the undeformed state. The residual vector without MOR is given by $\mathbf{G} = \mathbf{R}_{lin} + \mathbf{R}_{nl} - \mathbf{P}$ where \mathbf{P} is the external force vector. Since the linear component \mathbf{R}_{lin} can be well approximated with POD, DEIM is additionally applied to $\mathbf{R}_{nl}(\mathbf{U})$, as otherwise the full stiffness matrix for the nonlinear component would need to be recalculated for each time step. Applying POD and DEIM to the residual vector results in the following equation:

$$\mathbf{G}_{red}(\bar{\mathbf{U}}) := \mathbf{K}_{lin\ red} \mathbf{U}_{red} + \mathbf{R}_{nl\ red}(\bar{\mathbf{U}}) - \Phi_m^\top \mathbf{P} = \mathbf{0} \quad (30)$$

where $\mathbf{G}_{red}(\bar{\mathbf{U}})$ is the reduced residual vector obtained through POD and DEIM, $\mathbf{R}_{lin,red} = \mathbf{K}_{lin\ red}\mathbf{U}_{red}$ is the approximated linear component using POD,

$$\mathbf{R}_{nl\ red}(\bar{\mathbf{U}}) = \Phi_m^\top \Omega_k (\mathbf{Z}^\top \Omega_k)^{-1} \mathbf{Z}^\top \mathbf{R}_{nl}(\bar{\mathbf{U}}) \quad (31)$$

is the reduced nonlinear component obtained using DEIM and POD, and $\mathbf{P}_{red} = \Phi_m^\top \mathbf{P}$ is the reduced projection of the load using POD. This split was proposed by Radermacher et al. [25]. It is important to mention that in equation 31 most of the quantities are precomputed. This includes $\mathbf{K}_{lin\ red}$ and a large part of $\mathbf{R}_{nl\ red}(\bar{\mathbf{U}})$, which can be combined into the new matrix

$$\mathbf{M}_{DEIM} = \Phi_m^\top \Omega_k (\mathbf{Z}^\top \Omega_k)^{-1}. \quad (32)$$

These matrices are not recalculated in the reduced simulation and are constant throughout the computation. The matrix Φ_m is the matrix we get from the POD approach. New are the matrices Ω_k and \mathbf{Z}^\top . The matrix Ω_k is a projection matrix for the nonlinear internal force vector, and its interpretation is similar to that of the projection matrix used in POD. The matrix \mathbf{Z}^\top is the selection matrix and is composed of individual unit vectors, indicating which degrees of freedom and therefore which elements need to be evaluated. While the matrix $\mathbf{R}_{nl}(\bar{\mathbf{U}})$ still exists in its full dimension, the multiplication with \mathbf{Z}^\top determines which entries of $\mathbf{R}_{nl}(\bar{\mathbf{U}})$ are actually needed, and only those entries and their corresponding elements need to be evaluated.

Input: $D_R = [\mathbf{R}_{nl}(U(t_1)), \mathbf{R}_{nl}(U(t_2)), \dots, \mathbf{R}_{nl}(U(t_j))], k$

Output: Ω_k, \mathbf{Z}

$\Omega \Sigma \mathbf{V} = D_R$

$\Omega_k = [\omega_1, \omega_2, \dots, \omega_k]$

$[\rho, \gamma_1] = \max |\omega_1|$

$\mathbf{Z}_1 = [e_{\gamma_1}]$

for $i=1$ **to** $k-1$ **do**

$\mathbf{Z}_i^T \Omega_i \mathbf{c}_i = \mathbf{Z}_i^T \omega_{i+1}$
 $\mathbf{R}_{i+1} = \omega_{i+1} - \Omega_i \mathbf{c}_i$
 $[\rho, \gamma_i] = \max |\mathbf{R}_{i+1}|$
 $\mathbf{Z}_{i+1} = [\mathbf{Z}_i \ e_{\gamma_i}]$

end

Algorithm 1: DEIM algorithm for finding indices

To obtain the two matrices, we use the approach proposed by Chaturantabut and Sorensen [7], or Radermacher and Reese [25]. This is illustrated in Algorithm 1, where the snapshots of the nonlinear component of the internal force vector D_R and the desired number of DEIM modes k are used as input. By performing a SVD, the matrices $D_R = \Omega \Sigma \mathbf{V}$ are obtained. The first k vectors of the matrix $\Omega = [\omega_1, \omega_2, \dots, \omega_j]$ yield the projection matrix $\Omega_k = [\omega_1, \omega_2, \dots, \omega_k]$. The selection of discrete interpolation points is done in a greedy manner. In the initial step, the position γ_1 of the maximum value of the first DEIM mode is found as $[\rho, \gamma_1] = \max |\omega_1|$. Where ρ is the maximum value and γ_l the index which can be interpreted as the position with the corresponding degree of freedom. This position is chosen as the first interpolation point $\mathbf{Z}_1 = [e_{\gamma_1}]$. In the subsequent stages, the next DEIM mode is considered, and efforts are made to subtract the previously determined modes as efficiently as possible. This approach takes into account the directions in which significant knowledge already exists, allowing for the selection of interpolation points that provide new information. The exact formulas for this process are shown in Algorithm 1. Finally, the previously introduced residual vector eq. (30) is solved using the Newton-Raphson method. A time step of this process is shown in eq. 28. Using the DEIM in the field of finite element simulations with classically assembled meshes, it should be mentioned that determining the values at individual discrete points in the mesh is not straightforward. In this method, in order to evaluate the values at a single point, the adjacent elements need to be evaluated as well. Nevertheless, there are strategies available to overcome this issue and maintain the efficiency of the original DEIM method [1].

3.3 Arc-length method

As discussed in Chapter 2, the material model being considered exhibits softening behavior. This means that in a load-controlled simulation, the simulation can only run until the limit

load is reached at best. Further loading of the material does not result in equilibrium and no more solutions can be found. Displacement-controlled simulation is the simplest solution to this problem, allowing for simulation of the material beyond the limit load into the softening regime. However, this approach is not suitable for materials that exhibit snap-back behavior.

Snap-back is a phenomenon where not only the load decreases, but also the displacement, as shown in the exemplary load-displacement curve in Figure 1. Figure 1a illustrates the problem of load-controlled simulation, where no equilibrium state exists when the prescribed load becomes too large. Figure 1b visualizes the issues with displacement-controlled simulation, where a unique solution does not exist for the prescribed displacement u_6 .

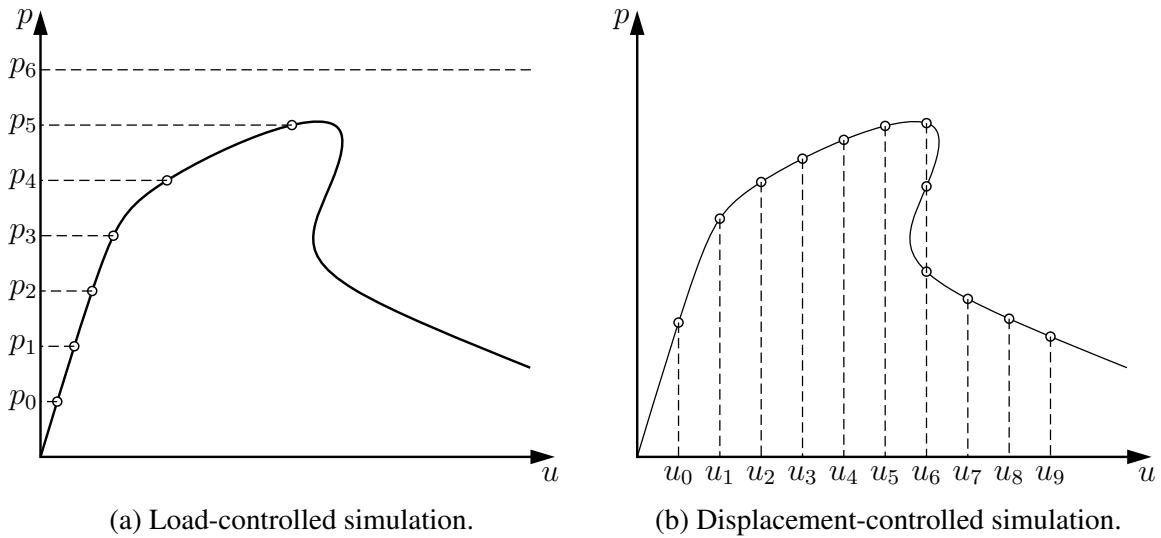


Figure 1: Limitations of standard load-controlled and displacement-controlled techniques.

To overcome these problems, the constant arc-length method was developed by Riks [27, 28] and Wempner [33], and made computationally efficient by Ramm [26] and Crisfield [10] in slightly different ways as shown in Fig. 2.

3.3.1 Modified Riks-Wempner method

Suppose that a solution exists from a previous pseudo-timestep $t - 1$ with ${}^{(t-1)}\mathbf{U} = {}^{(t)}\mathbf{U}^{(0)}$ and ${}^{(t-1)}\lambda = {}^{(t)}\lambda^{(0)}$, and we want to obtain the solution for the next pseudo-timestep ${}^{(t)}\mathbf{U}$ and ${}^{(t)}\lambda$. For simplicity, we will omit the left superscript for the pseudo-timestep t . We will indicate the iteration counter with a right superscript in brackets. At the beginning of the simulation (or at the first pseudo-timestep), we need to set a few parameters: the arc-length Δs_0 , the reference load \mathbf{P}_0 , and a predefined change in the load level $\Delta \lambda_0$. Once these parameters are set, we can initiate a new pseudo-timestep.

First, we increase the load level by the predefined change as follows:

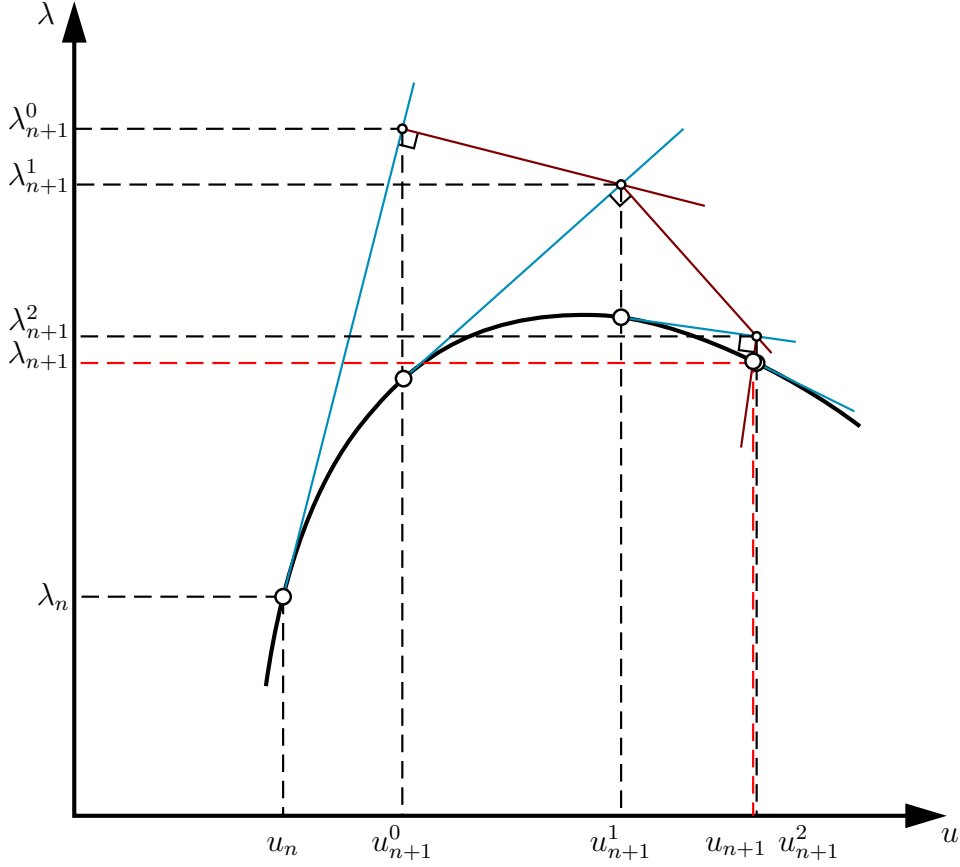


Figure 2: Visual representation of the arc-length method by Ramm.

$$\lambda = {}^{(t-1)}\lambda + \Delta\lambda_0. \quad (33)$$

Next, the tangential stiffness matrix $\mathbf{K}_T^{(0)}$ and the vector of internal forces $\mathbf{R}^{(0)}$ can be computed. Once these items have been computed and assembled, the vector of external forces $\mathbf{P}^{(0)}$ can be calculated as

$$\mathbf{P}^{(0)} = \mathbf{P}_0\lambda^{(0)}. \quad (34)$$

It's important to note that the external force vector $\mathbf{P}^{(0)}$ is determined by multiplying the reference load \mathbf{P}_0 by the current load factor $\lambda^{(0)}$.

This allows for the computation of the residual vector

$$\mathbf{G}^{(0)} = \mathbf{R}^{(0)} - \mathbf{P}^{(0)}. \quad (35)$$

With this, the linear system of equations can be solved to obtain the incremental displacement $\Delta\mathbf{U}^{(0)}$

$$\mathbf{K}_T^{(0)}\Delta\mathbf{U}^{(1)} = \mathbf{G}^{(0)}. \quad (36)$$

After calculating the current incremental displacement, the arc-length Δs of the pseudo-timestep can be determined

$$\Delta s = \|\Delta \mathbf{U}^{(1)}\|. \quad (37)$$

Another important aspect of the algorithm is handling the change of sign of $\Delta \lambda$ at limit points. To provide a comprehensive understanding for interested readers and facilitate the implementation of the method into a FEM code, the conditions for changing the sign will be explained as follows.

First, the stiffness parameter for the current pseudo-timestep needs to be computed

$$c = \Delta \mathbf{U}^{(1)\top} \mathbf{P}_0. \quad (38)$$

Next, we evaluate the ratio between the current stiffness parameter and the initial stiffness parameter:

$$r_c = \frac{{}^{(0)}c}{c}. \quad (39)$$

Assuming a positive stiffness parameter in the first pseudo-timestep, the ratio becomes negative when a limit point is passed, indicating that the current stiffness parameter has become negative. However, to ensure the generality of the implementation, we cannot rely solely on this ratio to determine the sign of $\Delta \lambda$. Instead, starting from the second pseudo-timestep, the following condition is used

$$r = \begin{cases} -\text{sgn}({}^{(t-1)}r) & \text{if } ({}^{(t-1)}r_c > 0 \text{ and } r_c < 0 \text{ and } ({}^{(t-1)}r_c < ({}^{(t-2)}r_c) \\ & \text{or } ({}^{(t-1)}r_c < 0 \text{ and } r_c > 0 \text{ and } ({}^{(t-1)}r_c > ({}^{(t-2)}r_c) \\ ({}^{(t-1)}r) & \end{cases} \quad (40)$$

In the first pseudo-timestep r is initiated as +1 and following that, r is either +1 or -1 depending on the aforementioned conditional statement. Having done all these steps, the correction of the load factor can be calculated as

$$\Delta \lambda^{(0)} = \frac{\Delta s_0}{\Delta s} * r. \quad (41)$$

The correction is added to the initial load factor at the beginning of the iteration leading to the load level for the next iteration

$$\lambda^{(1)} = \lambda^{(0)} + \Delta \lambda^{(0)} - \Delta \lambda_0 \quad (42)$$

Also, the the incremental change of the displacement vector is updated such that

$$\Delta \mathbf{U}_\lambda^{(1)} = \Delta \mathbf{U}^{(1)} * \Delta \lambda^{(0)} = \Delta \mathbf{U}_I. \quad (43)$$

The expression $\Delta \mathbf{U}_I$ for the incremental displacement of the first newton iteration of the pseudo-timestep is introduced for clarity, because it will be used in every Newton iteration after the first one. Lastly, the vector of unknowns can be updated

$$\mathbf{U}^{(2)} = \mathbf{U}^{(1)} + \Delta \mathbf{U}_\lambda^{(1)}. \quad (44)$$

For there on, the "normal" newton iteration ($i = 1, 2, \dots$) starts, beginning with the computation and assembly of the tangential stiffness matrix $\mathbf{K}_T^{(i)}$ and the vector of internal forces $\mathbf{R}^{(i)}$. From there on, the load vector can be calculated in dependency of the previously adjusted load factor

$$\mathbf{P}^{(i)} = \mathbf{P}_0 * \lambda^{(i)}. \quad (45)$$

Again, this will be used for the calculation of the residual vector

$$\mathbf{G}^{(i)} = \mathbf{R}^{(i)} - \mathbf{P}^{(i)}. \quad (46)$$

Following that, two incremental displacement vectors have to be calculated. The first is the result of solving

$$\mathbf{K}_T^{(i)} \Delta \mathbf{U}^{(i)} = \mathbf{G}^{(i)}. \quad (47)$$

for $\Delta \mathbf{U}^{(i)}$ and the second one is the result of solving

$$\mathbf{K}_T^{(i)} \Delta \mathbf{U}_{II}^{(i)} = \mathbf{P}_0 \quad (48)$$

for $\Delta^{(i)} \mathbf{U}_{II}$. These two solution vectors can now be used to calculate the new increment for the load factor

$$\Delta \lambda^{(i)} = - \frac{\Delta \mathbf{U}_I^T \Delta \mathbf{U}^{(i)}}{\Delta \mathbf{U}_I^T \Delta \mathbf{U}_{II}^{(i)}} \quad (49)$$

The increment is added to the load level from the beginning of the iteration to get the load level for the next iteration

$$\lambda^{(i+1)} = \lambda^{(i)} + \Delta \lambda^{(i)} \quad (50)$$

and also to update the increment of the displacement vector

$$\Delta \mathbf{U}_\lambda^{(i)} = \Delta \mathbf{U}^{(i)} + \Delta \lambda^{(i)} * \Delta \mathbf{U}_{II}^{(i)}. \quad (51)$$

Lastly, the displacement vector is updated for the next iteration

$$\mathbf{U}^{(i+1)} = \mathbf{U}^{(i)} + \Delta \mathbf{U}_\lambda^{(i)}. \quad (52)$$

This procedure from equation 45 on is repeated until the desired accuracy or the maximum number of iterations is reached. The method is also presented in algorithm 2 for a more compact overview. From the viewpoint of computational complexity, the second system of linear equations that has to be solved in every iteration doubles the CPU-time necessary to solve the

Input: ${}^{(t-1)}\mathbf{U}$, ${}^{(t-1)}\lambda$, Δs_0 , \mathbf{P}_0 , $\Delta\lambda_0$
Result: ${}^{(t)}\mathbf{U}$, ${}^{(t)}\lambda$
 Compute and assemble $\mathbf{K}_T^{(0)}$ and $\mathbf{R}^{(0)}$
 $\lambda^{(0)} = {}^{(t-1)}\lambda + \Delta\lambda_0$
 $\mathbf{P}^{(0)} = \mathbf{P}_0 * \lambda^{(0)}$
 $\mathbf{G}^{(0)} = \mathbf{R}^{(0)} - \mathbf{P}^{(0)}$
 $\mathbf{K}_T^{(0)} \Delta \mathbf{U}^{(t-1)} = \mathbf{G}^{(0)} \rightarrow$ solve for $\Delta \mathbf{U}^{(1)}$
 $\Delta s = \|\Delta \mathbf{U}^{(t-1)}\|$
 $c = \Delta \mathbf{U}^{(0)\top} \mathbf{P}_0$
 $r_c = \frac{{}^{(0)}c}{c}$
 $r = \begin{cases} -\text{sgn}({}^{(t-1)}r) & \text{if } ({}^{(t-1)}r_c > 0 \wedge r_c < 0 \wedge {}^{(t-1)}r_c < {}^{(t-2)}r_c) \\ & \vee ({}^{(t-1)}r_c < 0 \wedge r_c > 0 \wedge {}^{(t-1)}r_c > {}^{(t-2)}r_c) \\ {}^{(t-1)}r & \end{cases}$
 $\Delta\lambda^{(0)} = \frac{\Delta s_0}{\Delta s} * r$
 $\lambda^{(1)} = \lambda^{(0)} + \Delta\lambda^{(0)} - \Delta\lambda_0$
 $\Delta \mathbf{U}_\lambda^{(1)} = \Delta \mathbf{U}^{(t-1)} * \Delta\lambda^{(0)} = \Delta \mathbf{U}_I$
 $\mathbf{U}^{(2)} = \mathbf{U}^{(1)} + \Delta \mathbf{U}_\lambda^{(0)}$
for $i = 1$ **to** i_{max} **do**
 Compute and assemble $\mathbf{K}_T^{(i)}$ and $\mathbf{R}^{(i)}$
 $\mathbf{P}^{(i)} = \mathbf{P}_0 * \lambda^{(i)}$
 $\mathbf{G}^{(i)} = \mathbf{R}^{(i)} - \mathbf{P}^{(i)}$
 $\mathbf{K}_T^{(i)} \Delta \mathbf{U}^{(i)} = \mathbf{G}^{(i)} \rightarrow$ solve for $\Delta \mathbf{U}^{(i)}$
 $\mathbf{K}_T^{(i)} \Delta \mathbf{U}_{II}^{(i)} = \mathbf{P}_0 \rightarrow$ solve for $\Delta \mathbf{U}_{II}^{(i)}$
 $\Delta\lambda^{(i)} = -\frac{\Delta \mathbf{U}_I^\top \Delta \mathbf{U}^{(i)}}{\Delta \mathbf{U}_I^\top \Delta \mathbf{U}_{II}^{(i)}}$
 $\Delta \mathbf{U}_\lambda^{(i)} = \Delta \mathbf{U}^{(i)} + \Delta\lambda^{(i)} * \Delta \mathbf{U}_{II}^{(i)}$
 $\lambda^{(i+1)} = \lambda^{(i)} + \Delta\lambda^{(i)}$
 $\mathbf{U}^{(i+1)} = \mathbf{U}^{(i)} + \Delta \mathbf{U}^{(i)}$
 Check for convergence
end

Algorithm 2: Algorithmic solution scheme with the arc-length method applied.

system. This is one aspect of why it is of interest to implement model order reduction into the

arc-length method. Another aspect is the fact that in a DEIM-reduced simulation it is not possible to calculate some of the values in the full space because for example the stiffness matrix is only computed at interpolation points and can therefore not be used.

3.3.2 Reduced arc-length method

Having thoroughly explained the discrete empirical interpolation method and the 'full' Riks-Wempner arc-length method as proposed by Ramm, the implementation of the arc-length method in a reduced vector space is straight forward. It should be mentioned that a hyperreduction was already successfully applied to the the arc-length method proposed by Crisfield [10] by Lunay et al. [17], but to the knowledge of the author, hyperreduction has never been applied to Ramms arc-length method.

As explained in chapter 3.2, the stiffness matrix \mathbf{K}_T and the vector of internal forces \mathbf{R} are not fully computed, but only for the DOFs that were predefined in the offline step of the simulation. This means, that every value calculated in the arc-length method procedure is calculated from vectors and matrices in the reduced vector space.

Of course, everything stated concerning the offline step of the simulation are still applicable when the reduced arc-length method shall be used. This means that the matrices Φ_m , \mathbf{M}_{DEIM} and \mathbf{Z}^\top have been computed already.

Concerning the arc-length method part of the solution scheme, there are a few equations that are majorly influenced. These equations will be explained in the following.

First of all, equation 37 does actually not change, because the norm of the vector $\Delta\mathbf{U}$ is approximately equal to the norm of $\Delta\mathbf{U}_{red}$. This is due to the orthogonality of the basis vectors Φ_m and Ω_k . This means that the arc-length for pseudo-timestep t is the same whether it is computed in the reduced vector space or the full vector space. Because the vector $\Delta\mathbf{U}_{red}$ is solved in the reduced space, it can only be used to approximate the vector $\Delta\mathbf{U}$. Therefore, an approximation error is introduced to the arc-length of the pseudo-timestep. Going further the expression for the stiffness parameter c now reads

$$c = \Delta\mathbf{U}_{red}^{(0)\top} \mathbf{P}_{0red} \quad (53)$$

Again, the norm of both vectors is approximately equal to their norm in the full vector space and as a result, the dot product (represented by the matrix multiplication of both vectors, where the first one is transposed) leads to the same result in the reduced space as it would lead to in the original space. The steps after that are not changed in any way and as such, the reduced incremental displacement can be updated and added to the total reduced displacements such

that

$$\mathbf{U}_{red}^{(1)} = \mathbf{U}_{red}^{(0)} + \Delta\mathbf{U}_{\lambda red}^{(0)} \quad (54)$$

The solution must then be projected back to the full vector space, as it is necessary for the computation of the tangential stiffness matrix and the vector of internal forces. This is done via the conjuncture known from chapter 3.1

$$\mathbf{U}^{(1)} = \Phi_m \mathbf{U}_{red}^{(1)} \quad (55)$$

After the initial step is finished, the newton iteration starts. Again, the necessary entries of the tangential stiffness matrix and the internal force vector are computed and put into the desired form. From there, two reduced systems of linear equations are solved in order to calculate $\Delta\mathbf{U}_{red}^{(i)}$ and $\Delta\mathbf{U}_{II red}^{(i)}$. The two reduced systems of linear equations read

$$(\mathbf{K}_{lin red} + \mathbf{M}_{DEIM} \mathbf{Z}^\top \mathbf{K}_{T nl}^{(i)} \Phi_m) \Delta\mathbf{U}_{red}^{(i)} = \mathbf{G}_{red}^{(i)} \quad (56)$$

and

$$(\mathbf{K}_{lin red} + \mathbf{M}_{DEIM} \mathbf{Z}^\top \mathbf{K}_{T nl}^{(i)} \Phi_m) \Delta\mathbf{U}_{II red}^{(i)} = \mathbf{P}_{0 red}. \quad (57)$$

The obtained vectors are, similarly to equation 49, used to calculate the incremental load factor

$$\Delta\lambda^{(i)} = -\frac{\Delta\mathbf{U}_{I red}^\top \Delta\mathbf{U}_{red}^{(i)}}{\Delta\mathbf{U}_{I red}^\top \Delta\mathbf{U}_{II red}^{(i)}}. \quad (58)$$

This is then used to update the incremental displacement vector which is added to the vector of reduced unknowns. Similar to the initialization part of the pseudo-timestep, this vector is then projected to the full vector space so that the next iteration can take place. To highlight the differences of the full arc-length method and its reduced counterpart, the algorithmic form is shown in Algorithm 3, where all the equations and steps necessary for the implementation of a DEIM-reduced arc-length method are laid out.

Input: $(t-1)\mathbf{U}$, $(t-1)\mathbf{U}_{red}$, $(t-1)\lambda$, Δs_0 , \mathbf{P}_0 , $\Delta\lambda_0$

Result: $(t)\mathbf{U}$, $(t)\lambda$

Compute and assemble $\mathbf{K}_{Tred}^{(0)}$ and $\mathbf{R}_{red}^{(0)}$

$$\lambda^{(0)} = (t-1)\lambda + \Delta\lambda_0$$

$$\mathbf{P}_{red}^{(0)} = \mathbf{P}_{0red} * \lambda^{(0)}$$

$$\mathbf{G}_{red}^{(0)} = \mathbf{R}_{red}^{(0)} - \mathbf{P}_{red}^{(0)}$$

$$\mathbf{K}_{Tred}^{(0)} \Delta \mathbf{U}_{red}^{(0)} = \mathbf{G}_{red}^{(0)} \rightarrow \text{solve for } \Delta \mathbf{U}_{red}^{(0)}$$

$$\Delta s = \left\| \Delta \mathbf{U}_{red}^{(0)} \right\|$$

$$c = \Delta \mathbf{U}_{red}^{(0)\top} \mathbf{P}_{0red}$$

$$r_c = \frac{(0)c}{c}$$

$$r = \begin{cases} -\text{sgn}(r) & \text{if } ((t-1)r_c > 0 \wedge r_c < 0 \wedge (t-1)r_c < (t-2)r_c) \\ & \vee ((t-1)r_c < 0 \wedge r_c > 0 \wedge (t-1)r_c > (t-2)r_c) \\ (t-1)r & \end{cases}$$

$$\Delta\lambda^{(0)} = \frac{\Delta s_0}{\Delta s} * r$$

$$\lambda^{(1)} = \lambda^{(0)} + \Delta\lambda^{(0)} - \Delta\lambda_0$$

$$\Delta \mathbf{U}_{\lambda red}^{(0)} = \Delta \mathbf{U}_{red}^{(0)} * \Delta\lambda^{(0)} = \Delta \mathbf{U}_{Ired}$$

$$\mathbf{U}_{red}^{(1)} = \mathbf{U}_{red}^{(0)} + \mathbf{U}_{\lambda red}^{(0)}$$

$$\mathbf{U}^{(1)} = \Phi_m \mathbf{U}_{red}^{(1)}$$

for $i = 1$ **to** i_{max} **do**

 Compute and assemble $\mathbf{K}_{Tred}^{(i)}$ and $\mathbf{R}_{red}^{(i)}$

$$\mathbf{P}_{red}^{(i)} = \mathbf{P}_{0red} * \lambda^{(i)}$$

$$\mathbf{G}_{red}^{(i)} = \mathbf{R}_{red}^{(i)} - \mathbf{P}_{red}^{(i)}$$

$$\mathbf{K}_{Tred}^{(i)} \Delta \mathbf{U}_{red}^{(i)} = \mathbf{G}_{red}^{(i)} \rightarrow \text{solve for } \Delta \mathbf{U}_{red}^{(i)}$$

$$\mathbf{K}_{Tred}^{(i)} \Delta \mathbf{U}_{IIred}^{(i)} = \mathbf{P}_{red}^{(i)} \rightarrow \text{solve for } \Delta \mathbf{U}_{IIred}^{(i)}$$

$$\Delta\lambda^{(i)} = -\frac{\Delta \mathbf{U}_{Ired}^\top \Delta \mathbf{U}_{red}^{(i)}}{\Delta \mathbf{U}_{Ired}^\top \Delta \mathbf{U}_{IIred}^{(i)}}$$

$$\Delta \mathbf{U}_{\lambda red}^{(i)} = \Delta \mathbf{U}_{red}^{(i)} + \Delta\lambda^{(i)} * \Delta \mathbf{U}_{IIred}^{(i)}$$

$$\lambda^{(i+1)} = \lambda^{(i)} + \Delta\lambda^{(i)}$$

$$\mathbf{U}_{red}^{(i+1)} = \mathbf{U}_{red}^{(i)} + \Delta \mathbf{U}_{\lambda red}^{(i)}$$

$$\mathbf{U}^{(i+1)} = \Phi_m \mathbf{U}_{red}^{(i+1)}$$

 Check for convergence

end

Algorithm 3: Algorithmic solution scheme with the reduced arc-length method applied.

4 Numerical examples

In this section, we present two illustrative examples that demonstrate the possible application and the challenges of the so far proposed methods. These examples have been carefully chosen to showcase the model's capability to accurately predict the behavior of complex geometries

and loading conditions. At the same time the limitations of the methods are shown.

The first example focuses on a plate with a hole, a commonly encountered structural component closely related to various engineering applications. The presence of a hole significantly affects the stress distribution and fracture behavior, making it an ideal case to assess the reliability and accuracy of model order reduction methods. By investigating the response of this configuration, we aim to highlight the reduced order models ability to capture strain localization, and potential failure initiation and propagation.

The second example revolves around an asymmetrically notched specimen, which introduces an additional challenge due to the asymmetrical stress concentrations it induces. Notches are frequently encountered in structural components and can lead to significant stress concentration and failure initiation. By considering asymmetric notches, we aim to evaluate the model order reduction techniques in a highly challenging example.

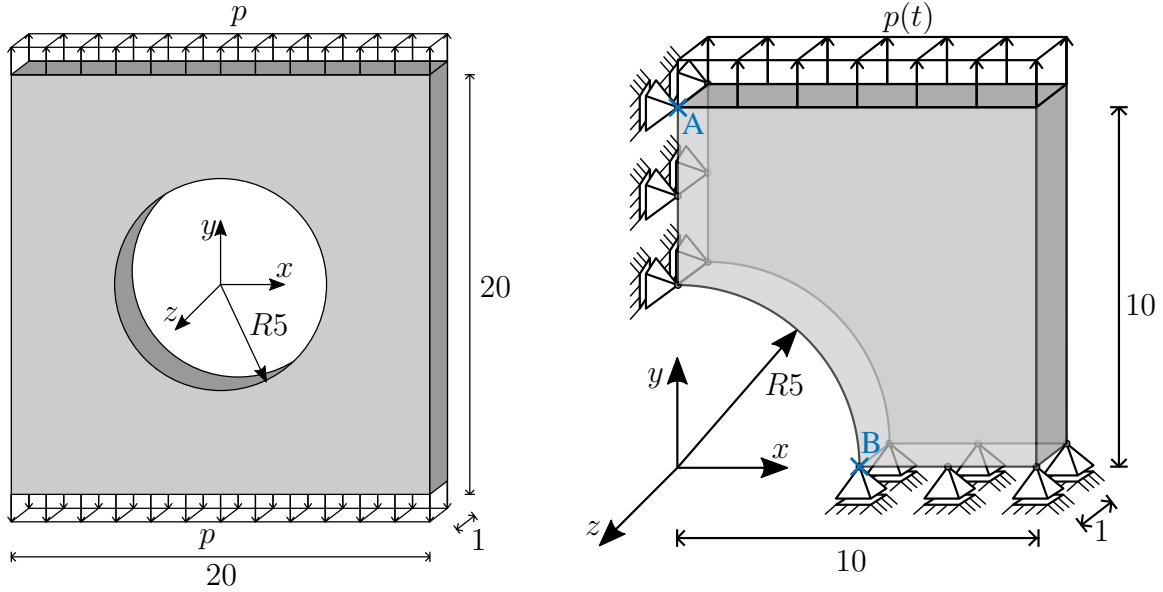
These examples will serve as valuable benchmarks for assessing the accuracy and applicability of our methods in practical scenarios, providing insights into the behavior of complex geometries and loading conditions. Through detailed analysis, we will demonstrate the model's ability to capture key mechanical phenomena, enabling engineers and researchers to make informed design decisions and enhance the reliability of their structural components.

4.1 Rectangular plate with a hole

The dimensions of the plate with a hole can be seen in Figure 3a. Due to the symmetry of the example, a quarter of the plate can be considered. This quarter is depicted in Figure 3b, along with the corresponding boundary conditions and applied loads.

The material parameters used for the simulations are listed in Table 1. These parameters are arbitrarily chosen, as the material parameters have not yet been fitted to experimental data. Therefore they have been chosen in such a way that both plasticity and damage develop in an intuitive way. Furthermore, efforts were made to ensure a complex material behavior, pushing the limits of the methods employed. It is important to note that the objective of this publication is not to investigate a specific material but rather to demonstrate the application of model reduction techniques to complex materials and more specifically gradient-extended models.

In the first step, mesh convergence is investigated to determine the number of elements required for a converged solution. This is done for the full simulation without any MOR. The load-displacement curves are shown in Figure 4. All four calculations were performed using 300 pseudo-timesteps, and the arc-length method was employed to control the load factor. It can be observed that the results converge as the mesh gets finer. Although the solution with 4804 elements has not fully converged, this mesh density is used for subsequent calculations. The limit



(a) Geometric configuration (dimensions in [mm]) (b) Quarter-Symmetry representation with applied boundary conditions and loads

Figure 3: Rectangular plate with a circular hole

load, denoted as p_{max} , represents the maximum load that can be applied to the structure, beyond which further loading is not possible. To compute the softening regime of the simulation, the arc-length method is used to reduce the load accordingly. For this example it could be calculated displacement-controlled. Due to the desired universal applicability of the methodology, the arc-length method is used nevertheless.

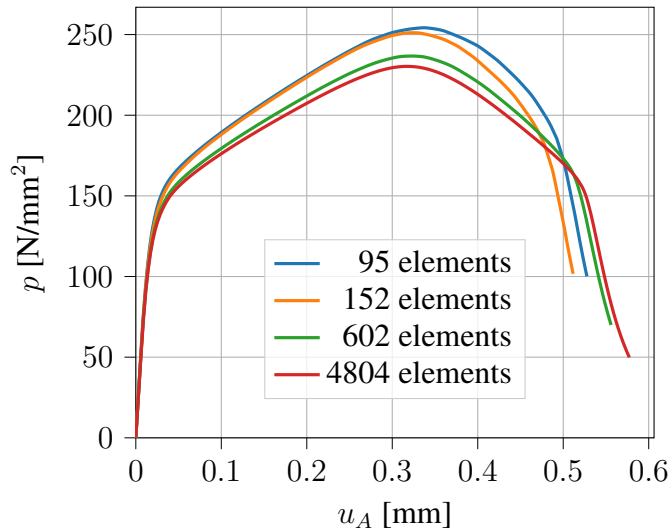


Figure 4: Mesh convergence study of the rectangular plate with a circular hole. u_a is the displacement in Point A shown in Figure 3b

The damage evolution for the various mesh densities under investigation is depicted in Figure 5. Thanks to the gradient-enhanced two-surface formulation, it can be observed, especially in

Symbol	Material parameter	Value	Unit
Λ	first Lamé parameter	75000	MPa
μ	second Lamé parameter	140000	MPa
σ_0	yield stress	325	MPa
a	first kinematic hardening parameter	2600	MPa
b	second kinematic hardening parameter	12.5	[-]
e	first isotropic hardening parameter	500	MPa
f	second isotropic hardening parameter	8	[-]
Y_0	damage threshold	10	MPa
r	first damage hardening parameter	0.5	MPa
s	second damage hardening parameter	1	MPa
A	internal length scale parameter	50	MPa mm ²
H	penalty parameter	10 ⁵	MPa

Table 1: Parameter set for the plate with a hole.

the finer meshes, that the damage does not only occurs in a single row of elements. In many damage formulations, a common issue is the limited band of damage, where the damage zone becomes narrower as the mesh becomes finer. This is not the case here. Nevertheless, the result seems to be not fully converged. However, since we will be comparing the solutions with the reference solution later on, the lack of convergence does not affect the investigation of the model reduction methods. Nonetheless, it is important to keep in mind that finer meshes would typically be required, leading to better speedups of the methods. To prevent lengthy calculations, we refrained from computing finer meshes.

4.1.1 Plasticity

Due to the complexity of the problem, we will investigate the different material behaviours in individual steps. In the first step, we will investigate purely plastic behavior. For this purpose, the damage threshold Y_0 will be set sufficiently high to prevent any damage initiation.

We will examine two different meshes, one with 602 elements and another with 4804 elements, to demonstrate the effectiveness of the methods for both meshes. Additionally, when considering the speedups later on, it will become evident how much more potential these methods hold when applied to larger and more complex models with significantly more elements. The force-displacement curves are presented in Figure 6. In each case, 200 snapshots were taken to construct the projection matrices.

To assess the quality of the reduced models, we compare them with the unreduced solution by examining the displacement at point A (see Figure 3b). We calculate the relative error between the unreduced and reduced solutions as follows:

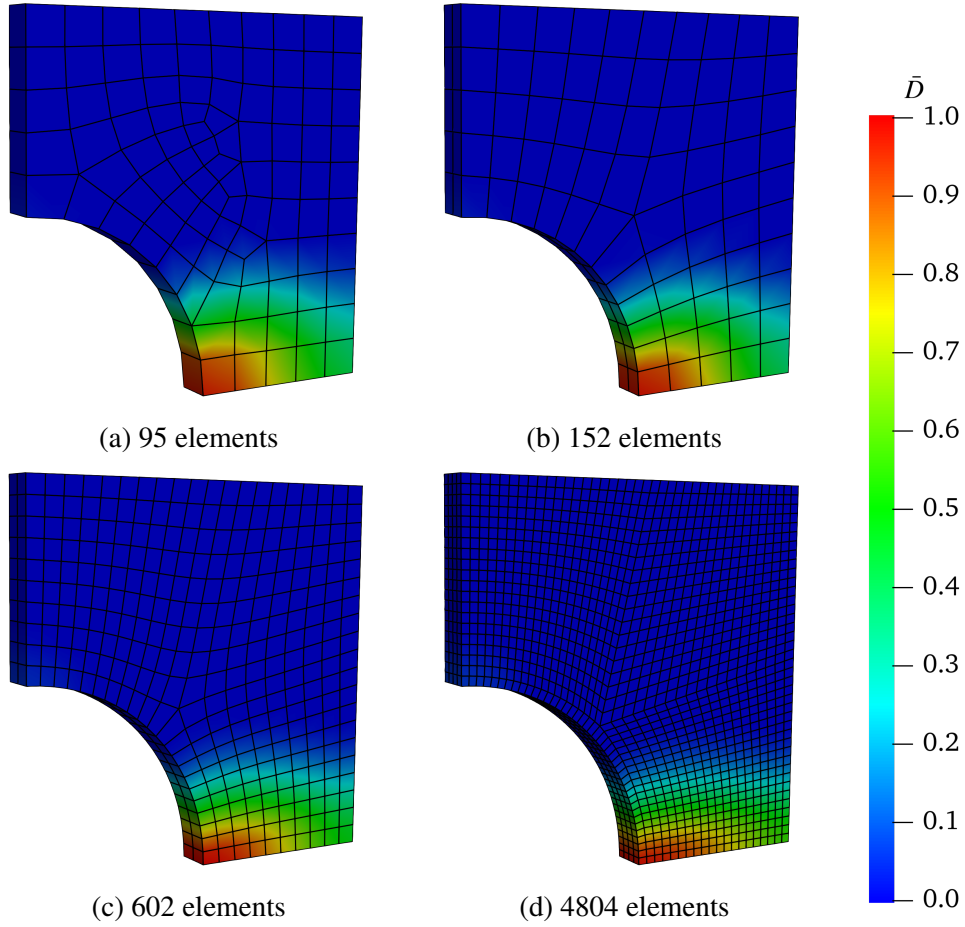


Figure 5: Damage of the specimen for the different meshes at the end of the simulation.

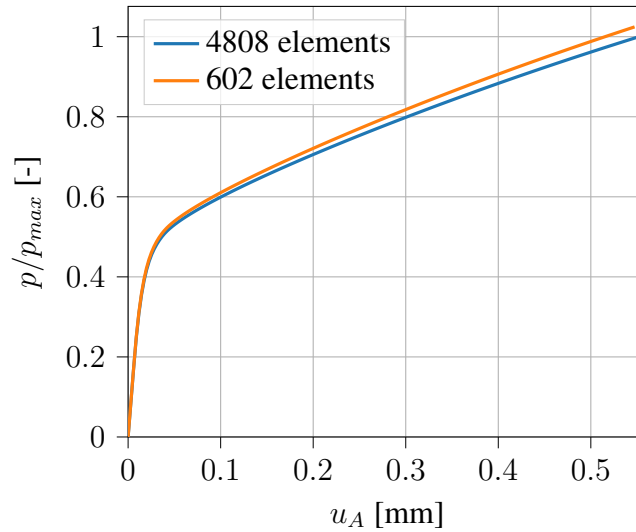


Figure 6: Load-displacement curve for an elastoplastic material behavior for 602 and 4808 elements of the full order model.

$$\varepsilon_{u_A} = \frac{|u_{A FOM} - u_{A DEIM}|}{u_{A prec}}. \quad (59)$$

where $u_{A\ FOM}$ represents the displacement at point A in the full order model (FOM) solution, and $u_{A\ DEIM}$ represents the displacement at point A in the reduced solution obtained through the DEIM method. In Figure 7, this error is plotted on the y-axis, while the number of DEIM modes used is shown on the x-axis. Since the number of POD modes was also varied, these will be represented by different curves (as indicated in the legend).

It can be seen that as the number of POD modes increases, the error decreases. While the simulations are getting more stable with increasing number of DEIM modes. With just 20 POD modes and 4 or more DEIM modes, an error of less than one percent can be achieved. However, it should be noted that the method becomes unstable with 3 DEIM modes. The cause of this instability is currently under investigation and cannot be reliably explained at present.

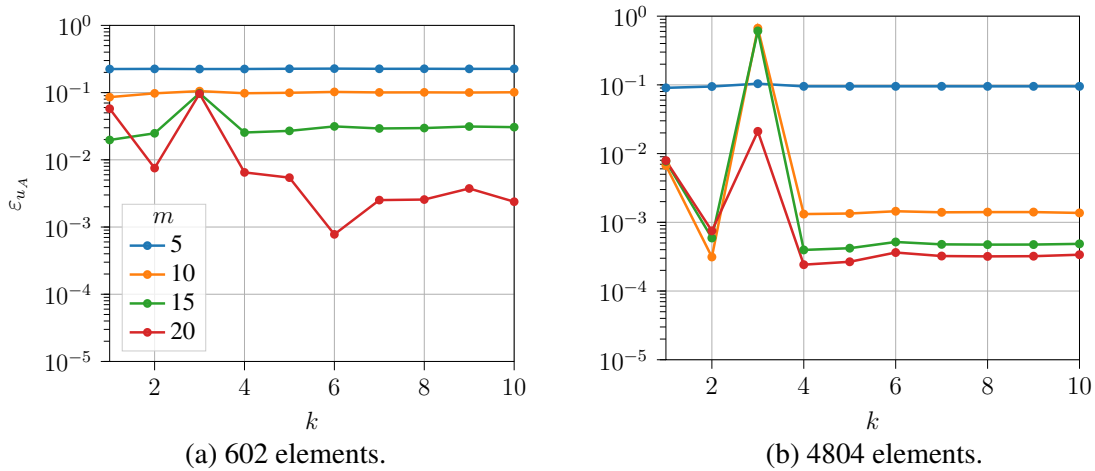


Figure 7: Approximation error for the elastoplastic case for the two different mesh discretizations.

An essential question that arises in the field of model reduction methods is the issue of speedups and how much time can be saved through these techniques. The speedup s_p is defined as

$$s_p = \frac{t_{full}}{t_{DEIM}} \quad (60)$$

with t_{full} is the time of one Newton step in the unreduced simulation and t_{DEIM} of the DEIM simulation including assembling and solving. In this publication, only academic examples with very few elements have been examined so far. Therefore, comparing different mesh densities is of interest. The mesh with 602 elements achieved a speedup of approximately 30, while the mesh with 4804 elements already achieved a speedup of about 170 as seen in Figure 8. This means that a calculation only requires around 0.6% of the time needed for the full calculation, while the error remains well below one percent. With larger examples, the speedups would be even better.

To demonstrate that it is not only the displacement at point A that is well approximated, Figure

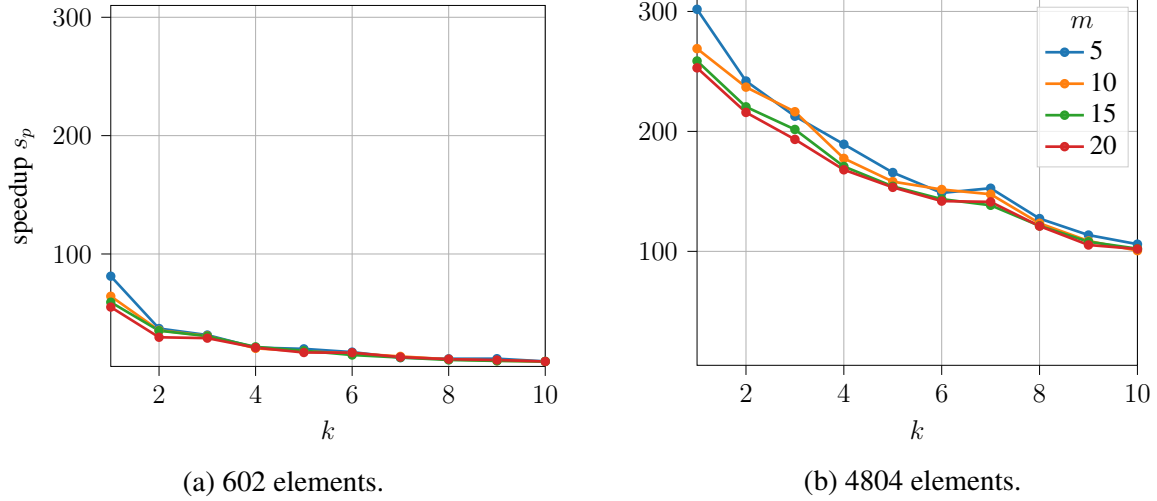


Figure 8: Speedup for the elastoplastic case for the two different mesh discretizations.

9 compares the force-displacement curve. For simplicity the force p is divided by p_{max} of the unreduced simulation. Due to the limited number of modes, there is a larger error in the elastic range, while the plasticity-dominated region is well approximated.

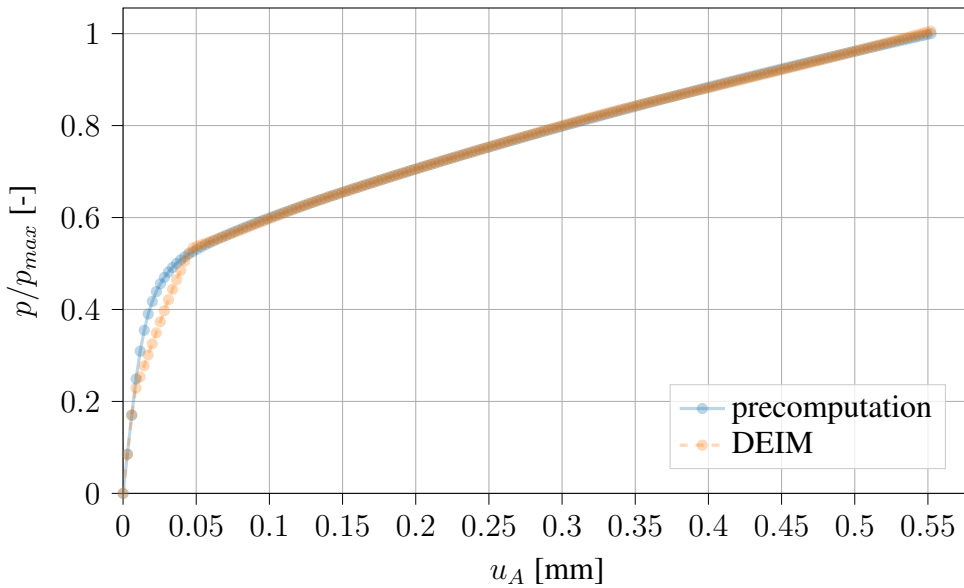


Figure 9: Load-displacement curves of the precomputation and the DEIM-reduced elastoplastic simulation with 20 POD modes and 4 DEIM modes.

4.1.2 Damage

In the next step, we will focus solely on damage analysis. To achieve this, we ensure that no plasticity occurs by setting the yield stress of plasticity to a very high value while the remaining parameters are the same as listed in 1. Furthermore, we will only perform calculations

using the mesh with 4804 elements. The force-displacement curve of the unreduced simulation is depicted in Figure 10. With the material model used, the plate with a hole can be simulated until complete failure occurs, resulting in a complete crack through the plate. However, performing a complete simulation with model reduction methods poses significant challenges. These complex phenomena include damage, unloading, and snapback behavior. For each of these phenomena, additional modes would be required. Since the presented method is kept very general, we have limited ourselves and will only simulate up to the 50th time step, which is beyond the limit load. In most practical applications, simulations are typically performed until a certain stress level is exceeded. Hence, we are already simulating well beyond what would be commonly employed in many fields.

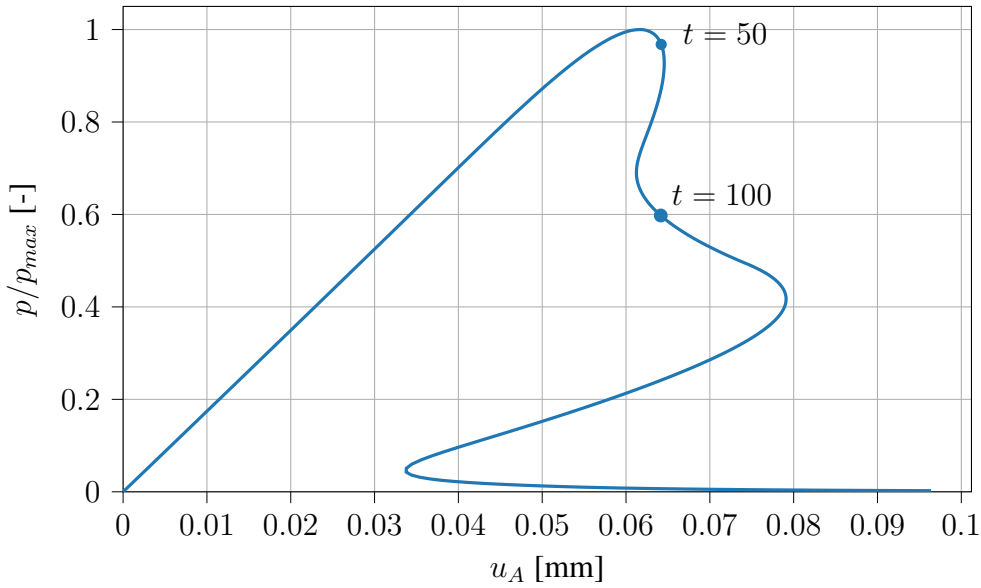


Figure 10: Force-displacement curve for an elasto-damage material behavior.

In addition to the relative displacement error, we introduce the relative error of the limit load

$$\varepsilon_{p_{max}} = \frac{|p_{max\ prec} - p_{max\ DEIM}|}{p_{max\ prec}} \quad (61)$$

where $p_{max\ prec}$ represents the limit load in the unreduced solution and $p_{max\ DEIM}$ represents the limit load in the reduced solution obtained through the DEIM method. The relative error of the maximum micromorphic damage

$$\varepsilon_{\bar{D}_B} = \frac{|D_{B\ prec} - D_{B\ DEIM}|}{D_{B\ prec}}. \quad (62)$$

where $D_{B\ prec}$ represents the maximum micromorphic damage in the unreduced solution and $D_{B\ DEIM}$ represents the maximum micromorphic damage in the reduced solution obtained through the DEIM method.

Figure 11 displays the error of the limit load. With 40 and 50 POD modes and a sufficient number of DEIM modes, the error can be reduced to the order of 10^{-6} . The displacement error

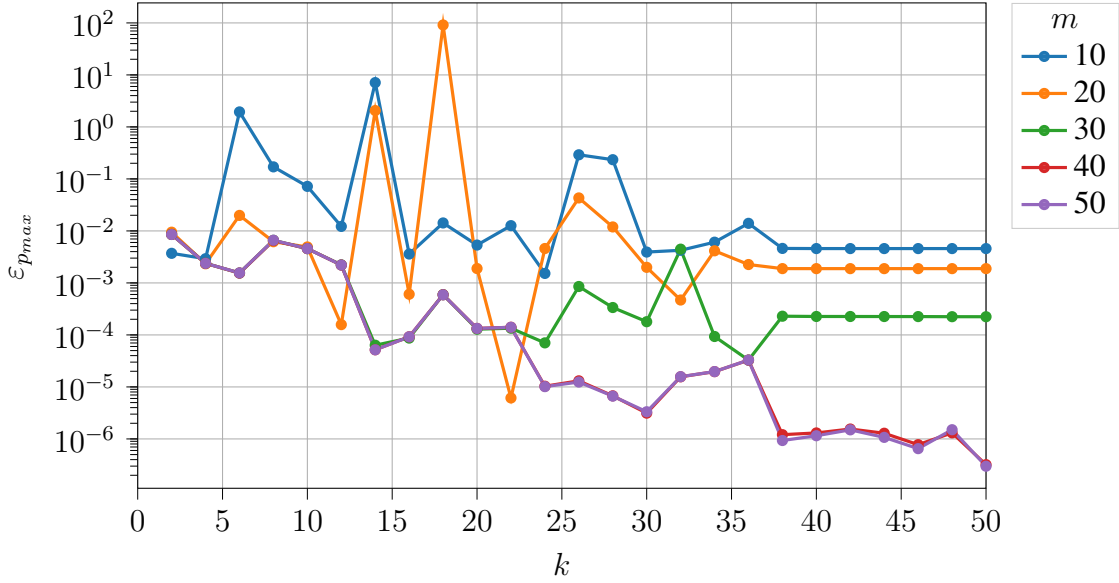


Figure 11: Relative error of the limit load with respect to the number of POD basis vectors m and the number of DEIM interpolation points k .

is depicted in Figure 12. There are simulations with very good results and errors on the order of 10^{-3} . However, there is no clear trend where the error consistently decreases with an increasing number of modes. This is due to an instability in the arc-length method, which needs to

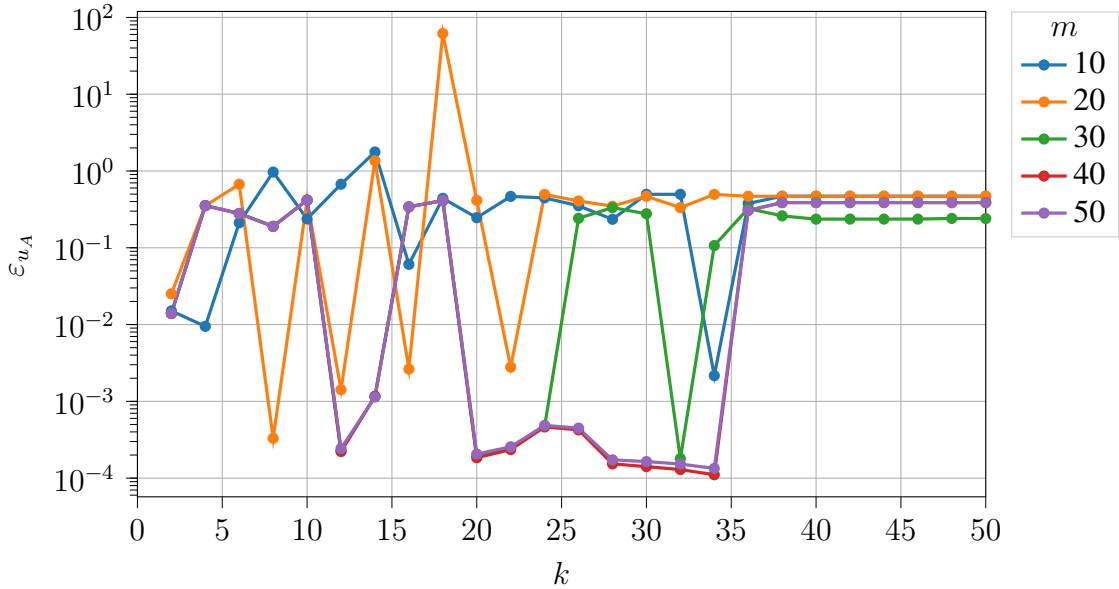


Figure 12: Relative error of the displacement in point A with respect to the number of POD basis vectors m and the number of DEIM interpolation points k .

be further investigated. The arc-length method follows the unloading path instead of continuing to load, leading to deviations. This is exemplified in Figure 13 for 40 POD modes and 40

DEIM modes. This problem of artificial unloading is already known. Pohl et al. investigated different path following schemes for problems with softening [23]. Their example of the constrained adaptive arc-length method did not converge with step size adjustment. Without step size adjustment a large number of increments are needed to trace the equilibrium path.

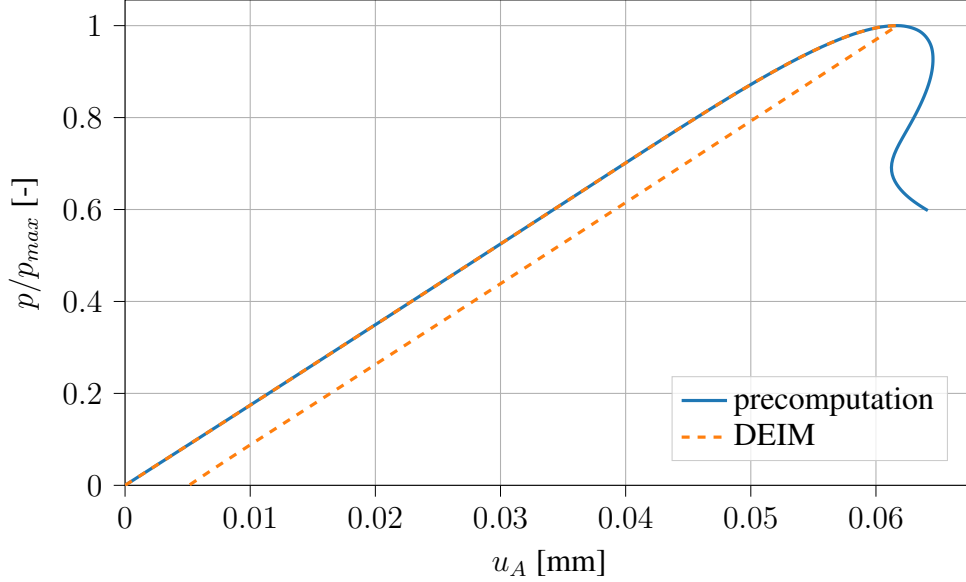


Figure 13: Comparison of the load-displacement curve of the precomputation and the DEIM-reduced simulation with 40 POD modes and 40 DEIM modes. There is an unintended occurrence of artificial unloading, which should be attempted to be avoided.

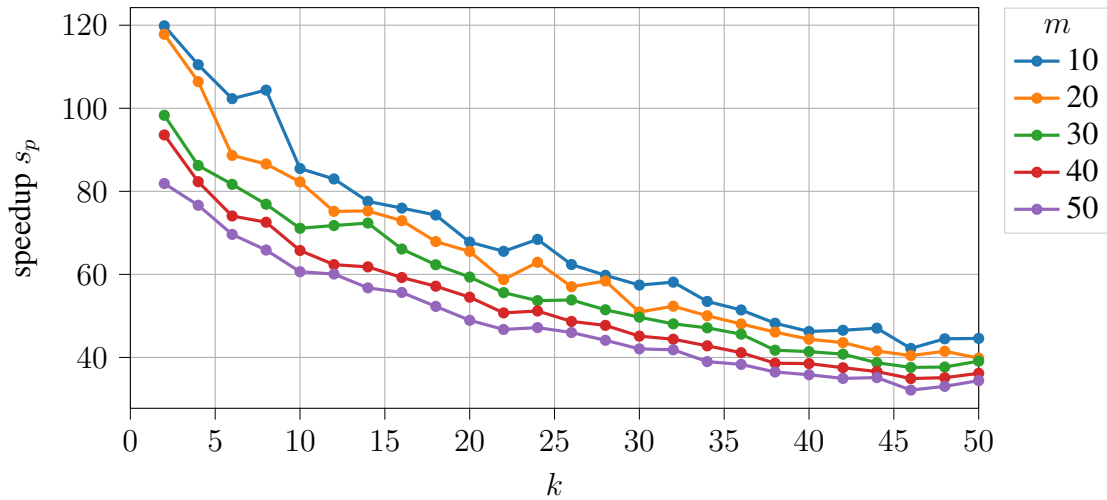


Figure 14: Speedup of the reduced simulation with respect to the number of POD basis vectors m and the number of DEIM interpolation points k for damage.

For completeness, a comparison of the speedups for the selected number of modes is presented. Even for this complex material behavior, speedups on the order of 40-80 can be achieved, as shown in Figure 14.

In Figure 15, the DEIM interpolation points selected by the Greedy algorithm are shown. Only the highlighted elements need to be evaluated which is really remarkable. The algorithm primarily selects elements from the region where damage occurs. Only after a sufficient number of elements from this region have been selected, the algorithm chooses elements from other regions.

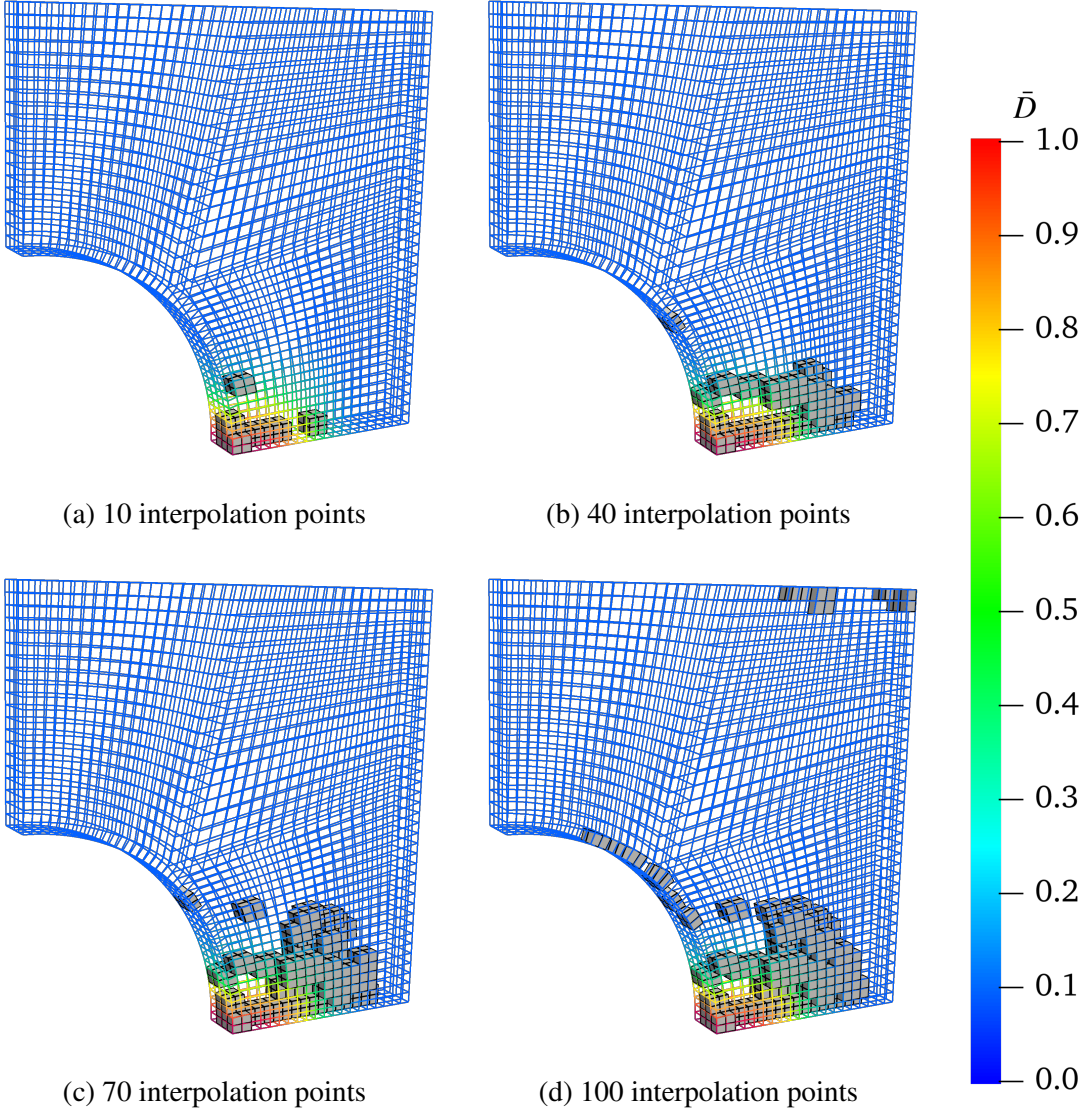


Figure 15: Elements that need to be evaluated in the reduced order model for different numbers of DEIM interpolation points.

4.1.3 Damage and plasticity

In this chapter, we examine the combination of plasticity and damage, using the material parameters from Table 1. The corresponding load-displacement curves have already been shown in Figure 4. Consequently, Figure 16 directly presents the relative error of the limit load. While

the error steadily decreases during the first 10 DEIM modes and is already below one percent, numerical instabilities and artificial unloading occur once again. However, for 50 and 70 POD modes, the error remains predominantly below one percent.

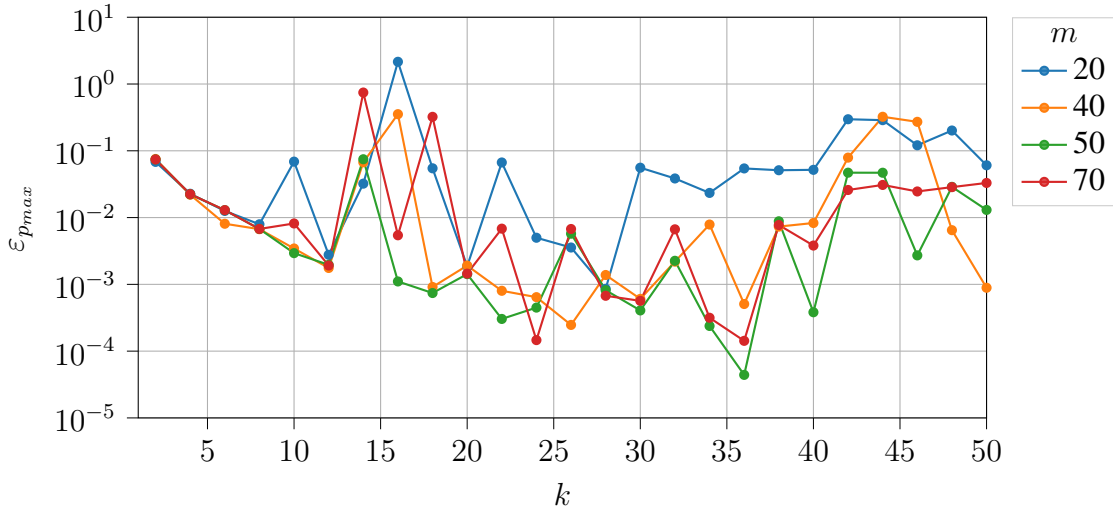


Figure 16: Relative error of the limit load with respect to the number of POD basis vectors m and the number of DEIM interpolation points k .

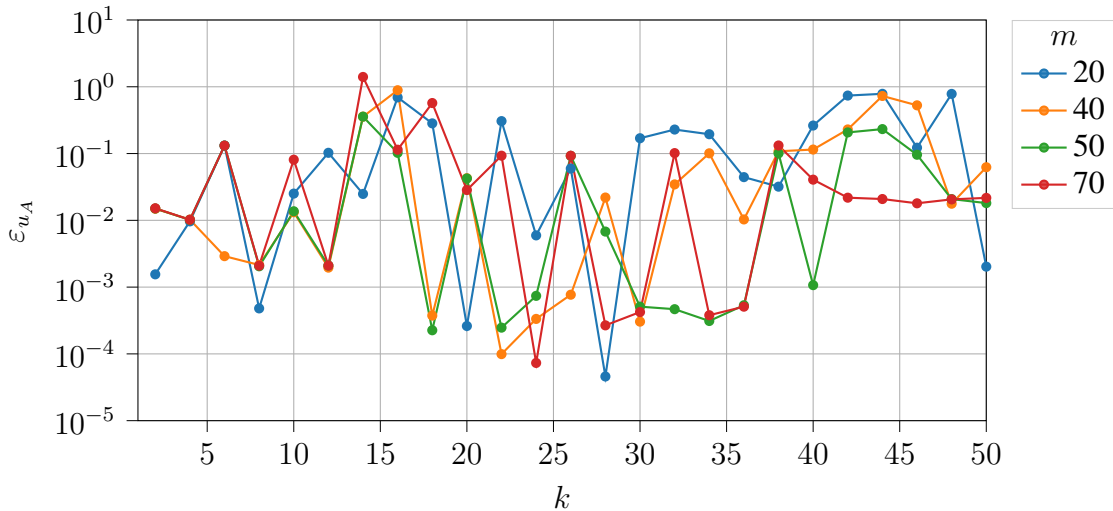


Figure 17: Relative error of the displacement in point A with respect to the number of POD basis vectors m and the number of DEIM interpolation points k .

For the displacement error (shown in Figure 17), there are also many results with very good accuracy.

However, the issue with the arc-length method arises once again, where it sometimes follows the unloading path instead of continuing to load further. As a result, the displacement at the end of the simulation is small and incorrect, even though the majority of the load-displacement curve can be approximated very well. This is exemplified in Figure 18.

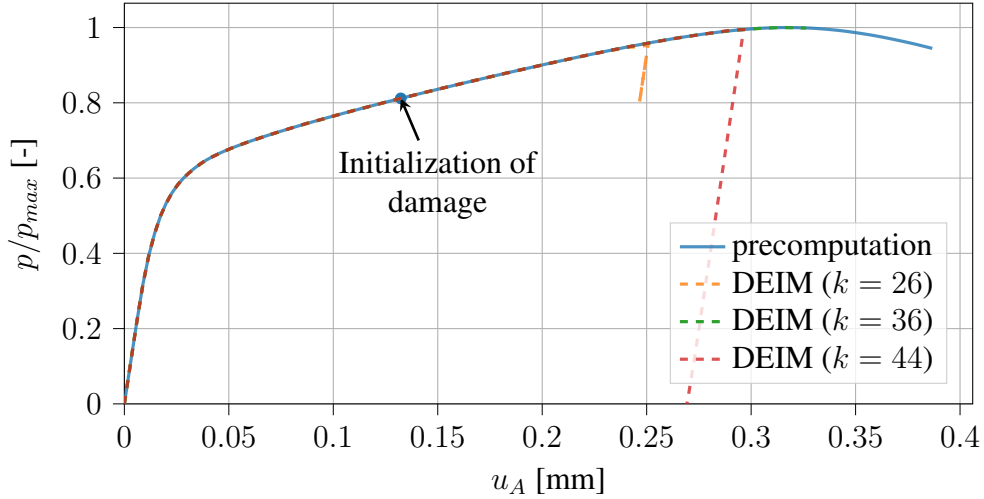


Figure 18: Comparison of the load-displacement curve of the precomputation and the DEIM-reduced simulation with 50 POD modes and 26, 36, and 44 DEIM modes.

Even for this complex material behaviour decent speedups can be achieved. The speedups s_p are shown in Figure 19. With 50 DEIM modes and 70 POD modes there is still a speedup of factor 15.52. This is because as the complexity of the material increases, the computation time for each individual element goes up, but at the same time, more time can be saved for each element that does not have to be calculated.

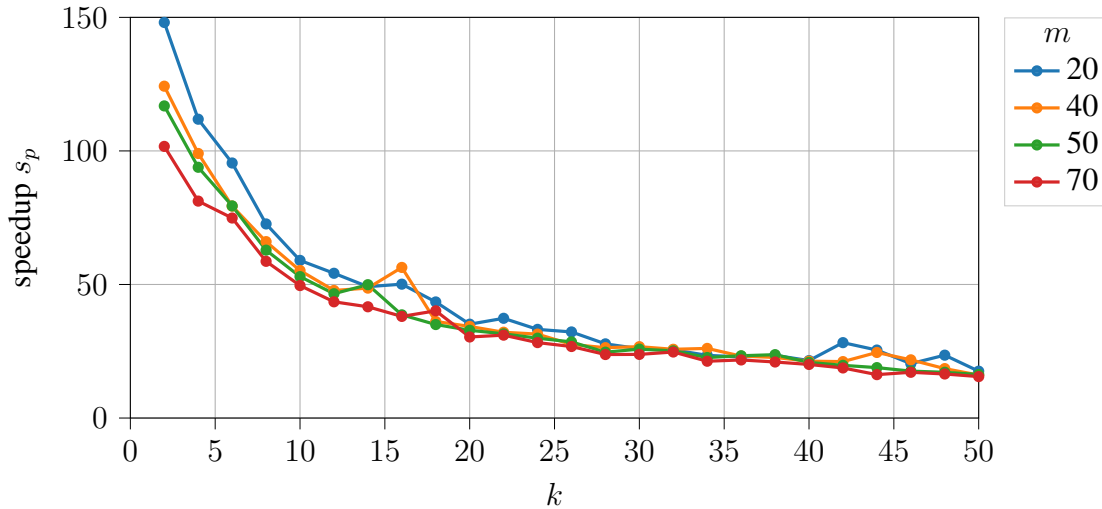
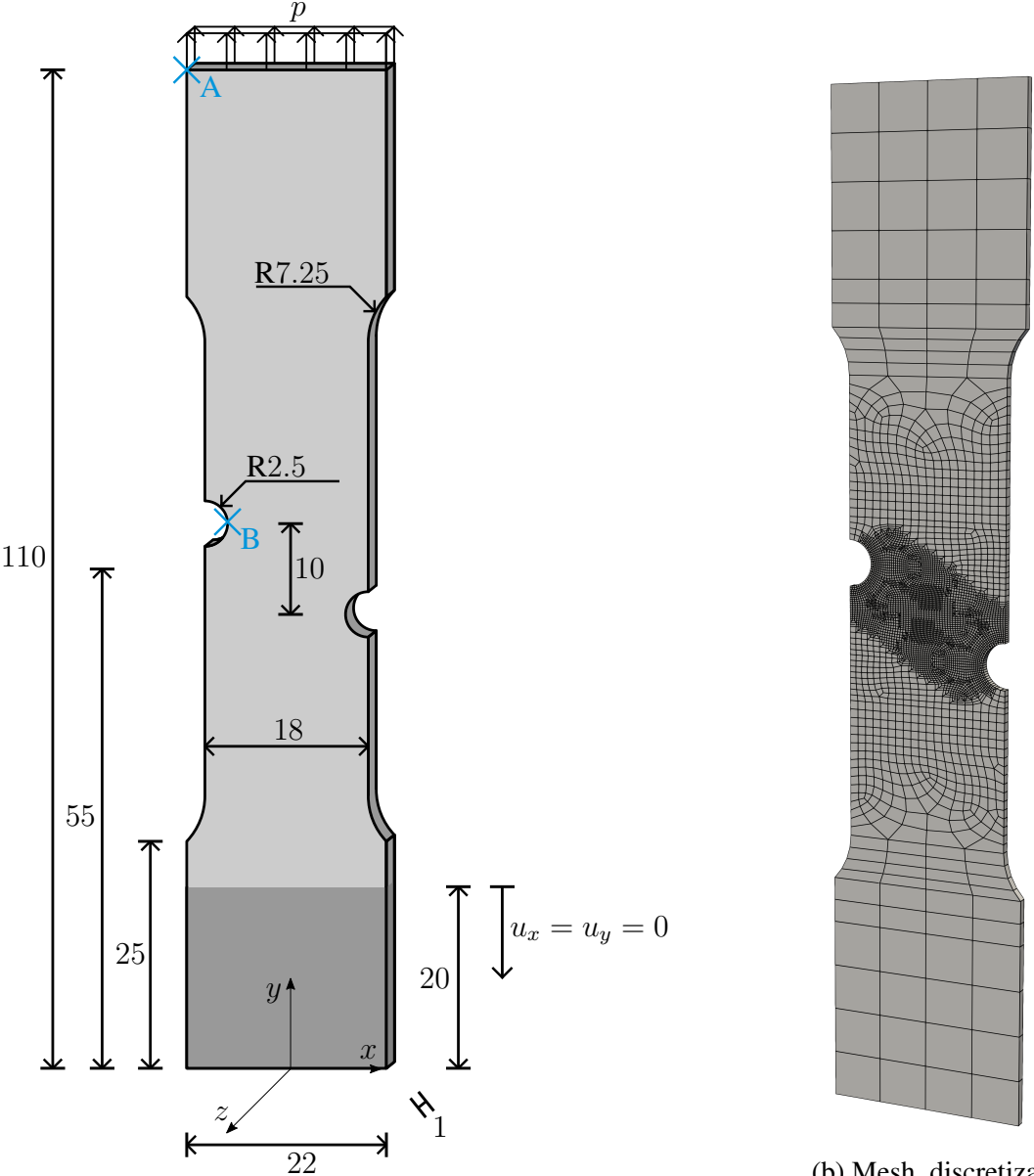


Figure 19: Speedup of the reduced simulation with respect to the number of POD basis vectors m and the number of DEIM interpolation points k for damage and plasticity.

4.2 Asymmetrically notched specimen

The second example is the asymmetrically notched specimen. In this case, no symmetry can be exploited. The corresponding dimensions can be seen in the drawing in Figure 20a. The

meshing is shown in Figure 20b. The mesh is refined in the area where damage and plasticity are expected to occur due to the geometric weakening. Since the structure is slightly more complex than the previous example, the material will be examined in three parts again. First, we will consider purely elastoplastic behavior before investigating damage without plasticity. In the final step, we will examine the behavior of plasticity and damage for this example as well. The general material parameters are listed in Table 2, based on the work of Brepols et al. [6].



(a) Geometry and boundary conditions of the asymmetrically notched specimen (dimensions in mm).

(b) Mesh discretization of the specimen.

Figure 20: Asymmetrically notched specimen.

Symbol	Material parameter	Value	Unit
Λ	first Lamé parameter	25000	MPa
μ	second Lamé parameter	55000	MPa
σ_0	yield stress	100	MPa
a	first kinematic hardening parameter	62.5	MPa
b	second kinematic hardening parameter	2.5	[-]
e	first isotropic hardening parameter	125	MPa
f	second isotropic hardening parameter	5	[-]
Y_0	damage threshold	2.5	MPa
r	first damage hardening parameter	5	MPa
s	second damage hardening parameter	100	MPa
A	internal length scale parameter	75	MPa mm ²
H	penalty parameter	10 ⁵	MPa

Table 2: Parameter set for the asymmetrically notched specimen.

4.2.1 Plasticity

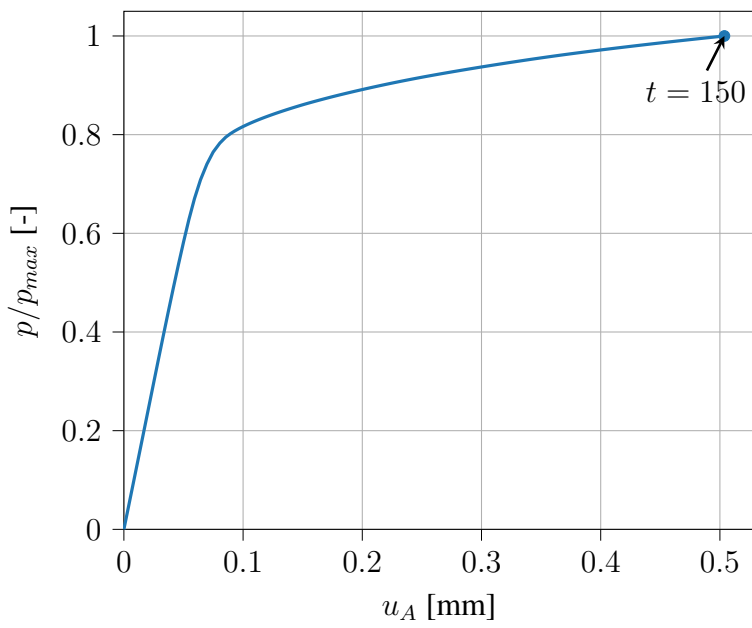
To examine only plasticity, the damage threshold σ_0 is again set to a high value to prevent any damage. The evolution of accumulated plastic strain is shown in Figure 21b. As expected, plastic deformation occurs between the two notches. The calculation was performed with 150 pseudo-timesteps, which were also used as snapshots for the reduced calculations. The load-displacement curve is depicted in Figure 21a.

Figure 22 shows the load-displacement curve for several reduced DEIM solutions along with the reference solution. It can be observed that with 20 POD bases and only a few DEIM bases, the behavior can be approximated very well. However, it should be noted that there are instabilities with DEIM in such complex behavior, as evident in the case of 20 POD bases and 4 DEIM bases. While it is usually expected that more DEIM bases would improve the solution, instabilities can also occur in this case.

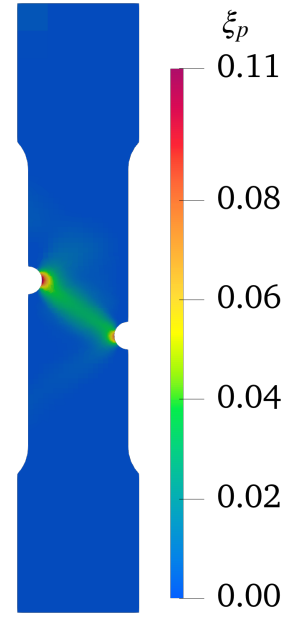
Figure 23a shows the displacement field in the y -direction for the DEIM computation with 20 POD modes and 3 DEIM bases. The elements that needed to be evaluated in the reduced computation are highlighted in green, while all other elements did not need to be evaluated. The reference solution from the unreduced precomputation is shown in Figure 23b, which looks identical.

4.2.2 Damage

Figure 24a shows the load-displacement curve for the case of damage without plasticity. The yield stress of plasticity has been set to a sufficiently high value to ensure that no plastic deformation occurs. The limit load is clearly exceeded in this case. The field of microstructural



(a) Force-displacement curve of the asymmetrically notched specimen for elasto-plastic material behavior.



(b) Accumulated plastic strain ξ_p after 150 pseudo-timesteps.

Figure 21: Simulation results of the asymmetrically notched specimen for elasto-plastic material behavior.

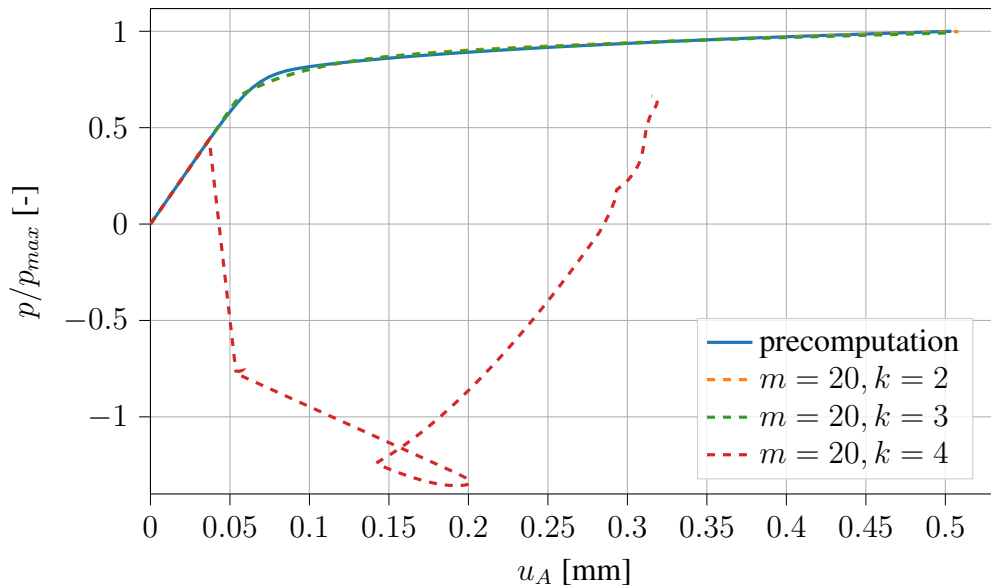
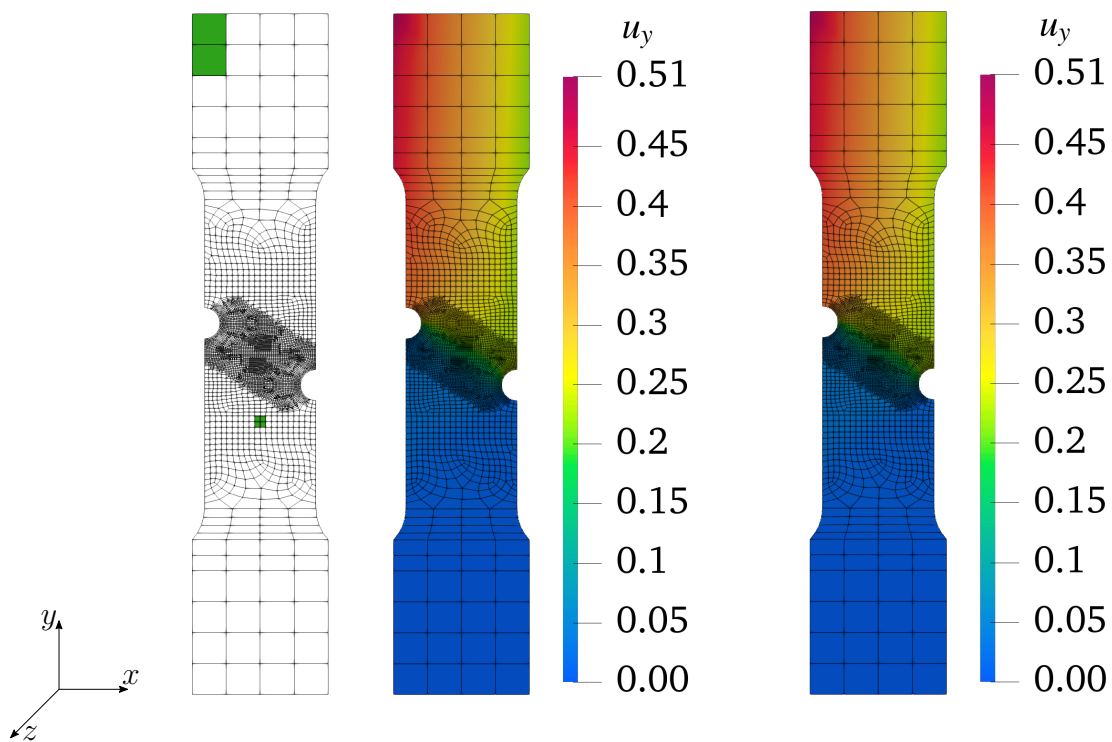


Figure 22: Load-displacement curves of the asymmetrically notched specimen for 20 POD modes and 2,3, and 4 DEIM modes compared to the precomputation.

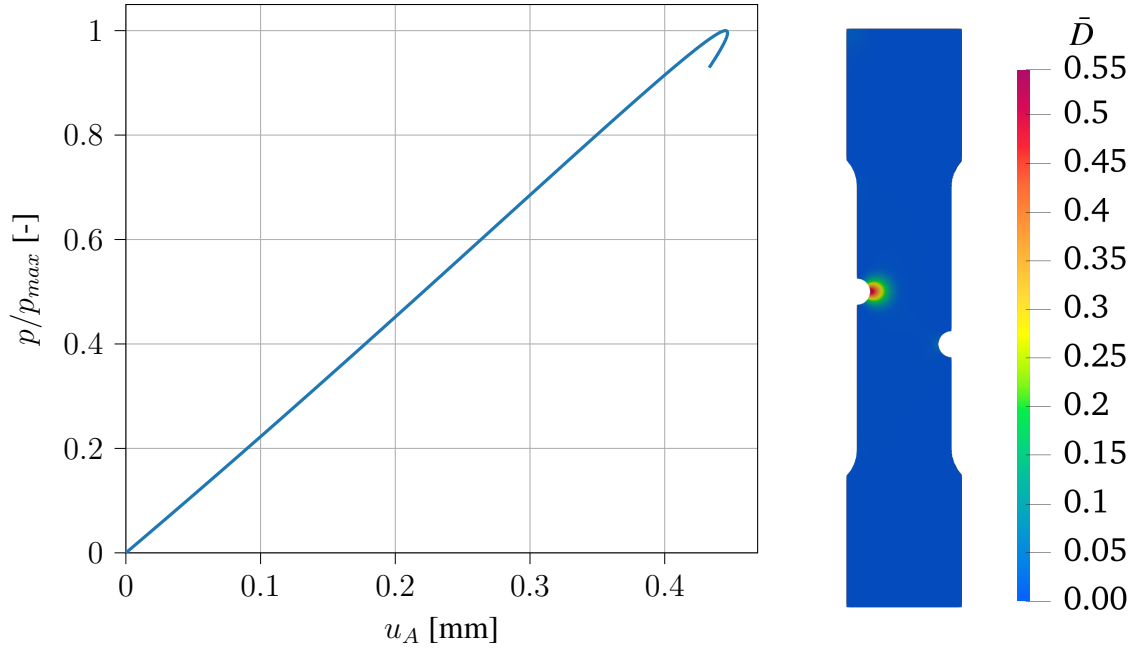
damage \bar{D} is shown in Figure 24b, where the initiation of damage can be observed in one of the notches, as expected.

Figure 25 shows the error in the limit load, while Figure 26 shows the error in the displace-



(a) DEIM elements and results with $k = 3$. (b) Displacements in y -direction at the end of the precomputation.

Figure 23: Results and DEIM elements for 3 DEIM interpolation points.



(a) Force-displacement curve of the asymmetrically notched specimen (b) Micromorphic damage \bar{D} after 150 pseudo-timesteps for micromorphic damage material behavior.

Figure 24: Simulation results of the asymmetrically notched specimen for micromorphic damage material behavior.

ment at point A. In both plots, it can be observed that with approximately 40 POD modes, the reduction methods are capable of reducing the error to below one percent. However, there are still some instabilities present. These instabilities did not improve even with a higher number of modes. Nevertheless, it can be seen from the load-displacement curves that the simulation follows the unloading path, allowing good and bad solutions to be distinguished even without a reference solution.

In this example, speedups of over 100 can be achieved. However, the actual speedup depends on the number of selected POD and DEIM modes. The specific speedups are shown in Figure 27. As a comparison, all the reduced calculations depicted here are still faster than a full-scale calculation.

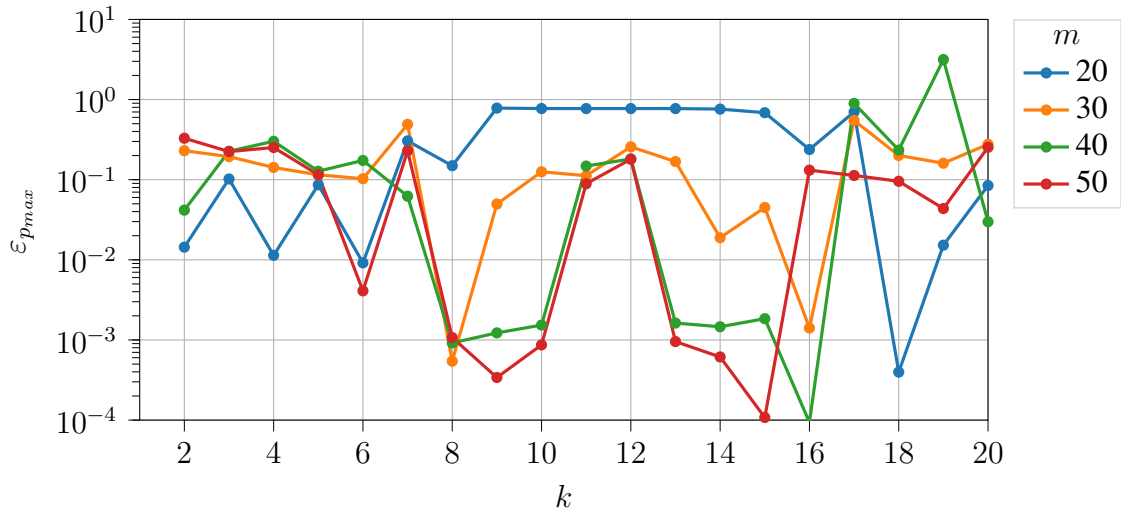


Figure 25: Relative error of the limit load with respect to the number of POD basis vectors m and the number of DEIM interpolation points k .

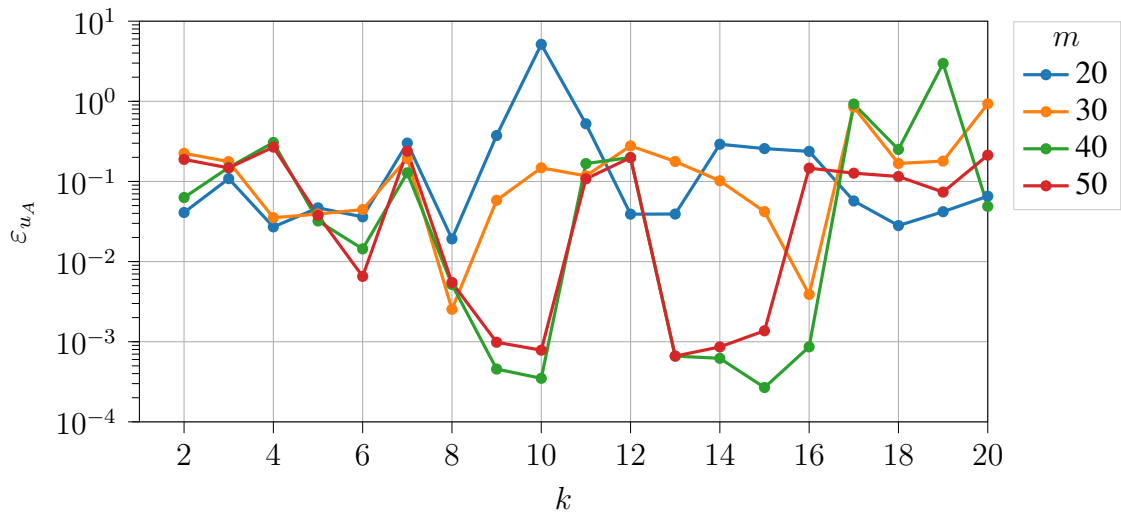


Figure 26: Relative error of the displacement in point A with respect to the number of POD basis vectors m and the number of DEIM interpolation points k .

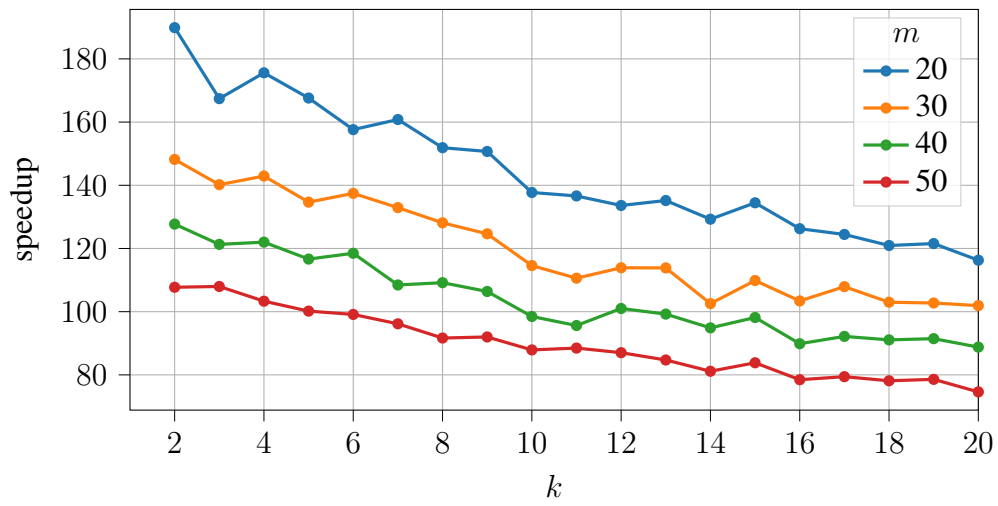


Figure 27: Speedup of the reduced simulation with respect to the number of POD basis vectors m and the number of DEIM interpolation points k .

4.2.3 Damage and plasticity

In the case of combining plasticity and damage, as expected, the difficulties and instabilities observed in the individual cases persist. In order to present a comprehensive picture, we include these challenges in this paper. The parameters used for this case are the same as those in Table 2. In Figure 28, we compare the load-displacement curves between the reference solution and reduced calculations using 40 POD modes with varying numbers of DEIM modes. While all the reduced calculations provide reasonably accurate results in the initial range, only a few modes are able to capture the plasticity region effectively. Overall, the methods were unable to produce satisfactory results beyond the limit load for such a complex problem.

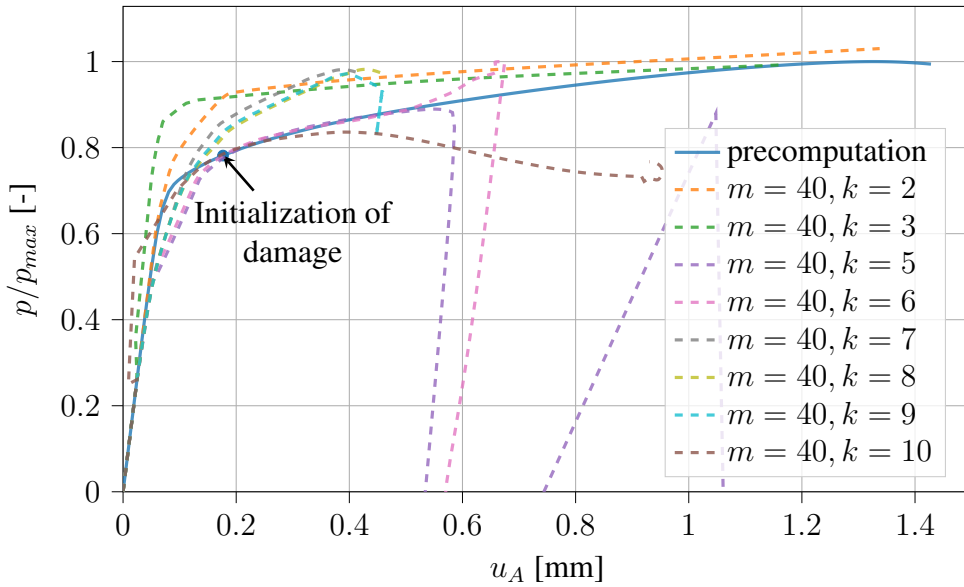


Figure 28: Comparison of the load-displacement curves of the precomputation with the curves of the ROM with 40 POD modes and an increasing number of DEIM modes.

This highlights the challenges in accurately capturing the combined behavior of plasticity and damage using reduced-order modeling techniques. Further investigation and development are required to address these instabilities and improve the reliability of the methods for such complex problems.

5 Conclusion

In conclusion, we have investigated the application of reduced-order modeling techniques for the simulation of plasticity and damage in structural problems. We have examined different scenarios, including the separate analysis of plasticity and damage, as well as their combination.

For plasticity analysis, we observed that with a sufficient number of POD modes and a small

number of DEIM modes, the behavior can be accurately approximated with errors below 1%. However, we also encountered numerical instabilities in the calculations, which require further investigation and refinement of the methods.

In the case of damage analysis without plasticity, we achieved good results with errors for the displacements in the range of 10^{-3} . The reduction in computational time was significant, with speedups ranging from 40 to 80 compared to full calculations.

When considering the combined effects of plasticity and damage, the challenges became more pronounced. Instabilities persisted even with higher numbers of POD and DEIM modes, making it difficult to obtain reliable and accurate results beyond the limit load.

Overall, the results demonstrate the great potential of reduced-order modeling for analyses involving highly nonlinear and complex material behaviors such as plasticity and damage, with significant computational speedups and accurate approximations achievable in many cases. Nevertheless, further research and development is still needed to address the observed instabilities in the study and to improve the robustness of the methods.

Acknowledgments

S. Kastian and S. Reese gratefully acknowledge the financial support of the project RE 1057/40 (project number 312911604) within SPP 1886 by the German Research Foundation (DFG). Furthermore, J. Kehls, T. Brepols and S. Reese acknowledge the financial support of subproject B05 within SFB/TRR 339 (project number 453596084) and S. Reese thankfully acknowledges the funding of subproject A01 within SFB/TRR 280 (project number 417002380) by the DFG. In addition, S. Reese and T. Brepols gratefully acknowledge the funding of the project RE 1057/51 (project number 453715964).

References

- [1] *A Modified Discrete Empirical Interpolation Method for Reducing Non-Linear Structural Finite Element Models* [2013], Vol. Volume 7B: 9th International Conference on Multi-body Systems, Nonlinear Dynamics, and Control of *International Design Engineering Technical Conferences and Computers and Information in Engineering Conference*.
- [2] Antil, H., Heinkenschloss, M. and Sorensen, D. C. [2014], ‘Application of the discrete empirical interpolation method to reduced order modeling of nonlinear and parametric systems’, *Reduced order methods for modeling and computational reduction* pp. 101–136.
- [3] Barfusz, O., Brepols, T., van der Velden, T., Frischkorn, J. and Reese, S. [2021], ‘A single gauss point continuum finite element formulation for gradient-extended damage at large deformations’, *Computer Methods in Applied Mechanics and Engineering* **373**, 113440.
- [4] Benner, P., Grivet-Talocia, S., Quarteroni, A., Rozza, G., Schilders, W. and Silveira, L. M. [2021], *System-and Data-Driven Methods and Algorithms*, De Gruyter.
- [5] Brepols, T., Wulfinghoff, S. and Reese, S. [2017], ‘Gradient-extended two-surface damage-plasticity: micromorphic formulation and numerical aspects’, *International Journal of Plasticity* **97**, 64–106.
- [6] Brepols, T., Wulfinghoff, S. and Reese, S. [2020], ‘A gradient-extended two-surface damage-plasticity model for large deformations’, *International Journal of Plasticity* **129**, 102635.
- [7] Chaturantabut, S. and Sorensen, D. C. [2010], ‘Nonlinear model reduction via discrete empirical interpolation’, *SIAM Journal on Scientific Computing* **32**(5), 2737–2764.
- [8] Chinesta, F., Ammar, A. and Cueto, E. [2010], ‘Recent advances and new challenges in the use of the proper generalized decomposition for solving multidimensional models’, *Archives of Computational methods in Engineering* **17**(4), 327–350.
- [9] Cooper, R., Popov, A. A. and Sandu, A. [2021], ‘Investigation of nonlinear model order reduction of the quasigeostrophic equations through a physics-informed convolutional autoencoder’, *arXiv preprint arXiv:2108.12344* .
- [10] Crisfield, M. A. [1981], A fast incremental/iterative solution procedure that handles “snap-through”, in ‘Computational methods in nonlinear structural and solid mechanics’, Elsevier, pp. 55–62.
- [11] Drmac, Z. and Gugercin, S. [2016], ‘A new selection operator for the discrete empirical interpolation method—improved a priori error bound and extensions’, *SIAM Journal on Scientific Computing* **38**(2), A631–A648.

- [12] Eivazi, H., Veisi, H., Naderi, M. H. and Esfahanian, V. [2020], ‘Deep neural networks for nonlinear model order reduction of unsteady flows’, *Physics of Fluids* **32**(10), 105104.
- [13] Fares, M., Hesthaven, J. S., Maday, Y. and Stamm, B. [2011], ‘The reduced basis method for the electric field integral equation’, *Journal of Computational Physics* **230**(14), 5532–5555.
- [14] Forest, S. [2009], ‘Micromorphic approach for gradient elasticity, viscoplasticity, and damage’, *Journal of Engineering Mechanics* **135**(3), 117–131.
- [15] Hernandez, J. A., Caicedo, M. A. and Ferrer, A. [2017], ‘Dimensional hyper-reduction of nonlinear finite element models via empirical cubature’, *Computer methods in applied mechanics and engineering* **313**, 687–722.
- [16] Idelsohn, S. R. and Cardona, A. [1985], ‘A reduction method for nonlinear structural dynamic analysis’, *Computer Methods in Applied Mechanics and Engineering* **49**(3), 253–279.
- [17] Launay, H., Besson, J., Ryckelynck, D. and Willot, F. [2021], ‘Hyper-reduced arc-length algorithm for stability analysis in elastoplasticity’, *International Journal of Solids and Structures* **208-209**, 167–180.
- [18] Mack, C. A. [2011], ‘Fifty years of moore’s law’, *IEEE Transactions on semiconductor manufacturing* **24**(2), 202–207.
- [19] Mourelatos, Z. P. [2000], ‘An efficient crankshaft dynamic analysis using substructuring with ritz vectors’, *Journal of Sound and vibration* **238**(3), 495–527.
- [20] Noor, A. K. and Peters, J. M. [1980], ‘Reduced basis technique for nonlinear analysis of structures’, *Aiaa journal* **18**(4), 455–462.
- [21] Nouy, A. [2010], ‘A priori model reduction through proper generalized decomposition for solving time-dependent partial differential equations’, *Computer Methods in Applied Mechanics and Engineering* **199**(23-24), 1603–1626.
- [22] Peherstorfer, B., Drmac, Z. and Gugercin, S. [2020], ‘Stability of discrete empirical interpolation and gappy proper orthogonal decomposition with randomized and deterministic sampling points’, *SIAM Journal on Scientific Computing* **42**(5), A2837–A2864.
- [23] Pohl, T., Ramm, E. and Bischoff, M. [2014], ‘Adaptive path following schemes for problems with softening’, *Finite elements in analysis and design* **86**, 12–22.
- [24] Radermacher, A. and Reese, S. [2013], ‘A comparison of projection-based model reduction concepts in the context of nonlinear biomechanics’, *Archive of Applied Mechanics* **83**(8), 1193–1213.

- [25] Radermacher, A. and Reese, S. [2016], ‘Pod-based model reduction with empirical interpolation applied to nonlinear elasticity’, *International Journal for Numerical Methods in Engineering* **107**(6), 477–495.
- [26] Ramm, E. [1981], Strategies for tracing the nonlinear response near limit points, in W. Wunderlich, E. Stein and K.-J. Bathe, eds, ‘Nonlinear Finite Element Analysis in Structural Mechanics’, Springer Berlin Heidelberg, Berlin, Heidelberg, pp. 63–89.
- [27] Riks, E. [1972], ‘The Application of Newton’s Method to the Problem of Elastic Stability’, *Journal of Applied Mechanics* **39**(4), 1060–1065.
- [28] Riks, E. [1979], ‘An incremental approach to the solution of snapping and buckling problems’, *International journal of solids and structures* **15**(7), 529–551.
- [29] Rocha, I. B. C. M., van der Meer, F. P. and Sluys, L. J. [2020], ‘An adaptive domain-based pod/ecm hyper-reduced modeling framework without offline training’, *Computer Methods in Applied Mechanics and Engineering* **358**, 112650.
- [30] Rozza, G. and Veroy, K. [2007], ‘On the stability of the reduced basis method for stokes equations in parametrized domains’, *Computer methods in applied mechanics and engineering* **196**(7), 1244–1260.
- [31] Ryckelynck, D., Lampoh, K. and Quilicy, S. [2016], ‘Hyper-reduced predictions for life-time assessment of elasto-plastic structures’, *Meccanica* **51**, 309–317.
- [32] San, O. and Maulik, R. [2018], ‘Neural network closures for nonlinear model order reduction’, *Advances in Computational Mathematics* **44**, 1717–1750.
- [33] Wempner, G. A. [1971], ‘Discrete approximations related to nonlinear theories of solids’, *International Journal of Solids and Structures* **7**(11), 1581–1599.
- [34] Willcox, K. [2006], ‘Unsteady flow sensing and estimation via the gappy proper orthogonal decomposition’, *Computers & fluids* **35**(2), 208–226.